International Journal of Heat and Fluid Flow 000 (2016) 1–20

Contents lists available at ScienceDirect

International Journal of Heat and Fluid Flow

journal homepage: www.elsevier.com/locate/ijhff

A level-set model for thermocapillary motion of deformable fluid particles

Néstor Balcázar*, Joaquim Rigola, Jesús Castro, Assensi Oliva*

Heat and Mass Transfer Technological Center (CTTC), Universitat Politècnica de Catalunya - BarcelonaTech (UPC) ETSEIAT, Colom 11, 08222 Terrassa (Barcelona), Spain

ARTICLE INFO

Article history:
Available online xxx

Keywords:
Thermocapillary
Variable surface tension
Interfacial heat transfer
Fluid particles
Conservative level-set method

ABSTRACT

A new level-set model is proposed for simulating immiscible thermocapillary flows with variable fluid-property ratios at dynamically deformable interfaces. The Navier–Stokes equations coupled with the energy conservation equation are solved by means of a finite-volume/level-set approach, adapted to a multiple marker methodology in order to avoid the numerical coalescence of the fluid particles. The temperature field is coupled to the surface tension through an equation of state. Some numerical examples including thermocapillary driven convection in two superimposed fluid layers, and thermocapillary motion of single and multiple fluid particles are computed using the present method. These results are compared against analytical solutions and numerical results from the literature as validations of the proposed model.

1. Introduction

When a fluid particle (bubble or drop) is placed in a second fluid in which a temperature gradient is imposed, it will move from the region with lower temperature to that with higher temperature so that the surface energy is minimized, due to the surface tension is usually a decreasing function of increasing temperature. This effect is called thermocapillary or Marangoni migration. It arises as a consequence of the local surface tension gradients on the fluid–fluid interface caused by temperature distribution. In addition to its importance from a fundamental point of view, it provides a particularly attractive means for manipulation of continuous fluid streams or fluid particles, in applications involving microgravity (Subramanian and Balasubramaniam, 2001) or microdevices (Darhuber and Troian, 2005; Karbalaei et al., 2016).

The thermocapillary migration of a drop was first examined experimentally by Young et al. (1959), who also found an analytical expression for the terminal velocity of a single spherical drop in the creeping flow limit, in which convective transport of momentum and heat can be neglected. They derived the named YGB theory for the prediction of the steady state migration velocity. The analysis of Young et al. (1959) was extended by Subramanian (1981) and Subramanian (1983), who studied the migration velocity of a non-deformable gas bubble and liquid droplet in the limit of zero Reynolds number. Since then, many works have been performed experimentally, analytically and numerically; most of the research on this phenomenon has been summarized by Subramanian and Balasubramaniam (2001).

Collections of fluid particles are usually encountered in practical applications, and the interaction between them will be more important. Thus, the thermocapillary motion of multiple spherical drops and their interactions has been studied by Anderson (1985) and Keh and Chen (1990; 1992) using analytical and combined analytical-numerical methods, in the limit of zero Reynolds and Marangoni numbers. Zhang and Davis (1992) studied the pairwise collision rate of small spherical drops undergoing thermocapillary migration in a dilute dispersion using a trajectory analysis. Sun and Hu (2002) reported a theoretical study of the thermocapillary motion of two bubbles along their line of centers in a uniform temperature gradient, whereas Yin and Li (2015) presented a numerical study on the interaction of two unequal and non-merging spherical drops using an axisymmetric model. These studies demonstrated that the collective behavior of multiple droplets is different from that of a single isolated drop. Further works have been reported on the Marangoni migration of droplets in the presence of neighboring boundaries, for instance Meyyappan et al. (1981) and Sadhal (1983) solved the quasi-steady problem of thermocapillary motion of a spherical gas bubble normal to an infinite planar solid or free fluid surface of constant temperature, (Meyyappan and Subramanian, 1987) examined the thermocapillary motion of a gas bubble parallel to a rigid planar surface, (Keh et al., 2002) have obtained numerical solutions and approxi-

* Corresponding authors. Fax: +(34) 93 739 89 20.
E-mail addresses: nestor@cttc.upc.edu, nestorbalcazar@yahoo.es (N. Balcázar), cttc@cttc.upc.edu (A. Oliva).

http://dx.doi.org/10.1016/j.ijheatfluidflow.2016.09.015
0142-727X/

mate analytical solutions for the steady thermocapillary motion of a fluid droplet parallel to two walls using a boundary collocation method and the method of reflexions, whereas (Chang and Keh, 2006) extend previous work to the motion of a fluid drop perpendicular to two walls. In these cases the migration velocity was found to decrease relative to the value given by Young et al. (1959).

The majority of the aforementioned investigations assume a fixed spherical shape for the migrating bubble or drop, however, this assumption is valid only in the limit of large surface tension, without convective transport of momentum and energy. Therefore, some numerical models have been proposed in order to solve these issues. For instance, Haj-Hariri et al. (1997) reported three-dimensional computations of the thermocapillary motion of deforming droplet based on a continuum model for the fluid–fluid interface, whereas Nas and Tryggvason (2003) and Nas et al. (2006) have performed comprehensive numerical simulations of the thermocapillary motion of multiple deformable droplets by means of the front-tracking (FT) method (Tryggvason et al., 2001). Maa and Bothe (2011) and Samareh et al. (2014) presented direct simulations of thermal Marangoni effects at dynamically deformable interface of two-phase incompressible fluids, based on modified versions of the volume-of-fluid (VOF) method (Hirt and Nichols, 1981). Yin et al. (2012; 2008) studied an isolated spherical drop in thermocapillary migration for low and high Marangoni numbers using a front-tracking scheme. Brady et al. (2011) and Zhao et al. (2010) reported simulations of the thermocapillary motion of two- and three-dimensional fluid particles using the level-set (LS) method (Osher and Sethian, 1988; Sussman et al., 1994). Guo and Lin (2015) have presented a phase-field (PF) model for binary incompressible fluid with thermocapillary effects, which was used to compute thermocapillary convection in a two-layer fluid system and thermocapillary migration of a drop.

To the best of the authors' knowledge, there are not previous works on the numerical modeling of two-phase flows with variable surface tension by means of the conservative level-set (CLS) method (Balcázar et al., 2014; Olsson and Kreiss, 2005), moreover, most of numerical research reported in the literature on thermocapillary motion of multiple deformable fluid particles has been performed by means of the front-tracking method (Nas et al., 2006; Nas and Tryggvason, 2003; Tryggvason et al., 2001), so that the capability and accuracy of new interface capturing methods for simulating this phenomena is still to be proven. Therefore, it is the purpose of this work to develop a sufficiently general numerical technique for simulating thermocapillary motion of deformable fluid particles, so that effects such as heat convection, container walls or the presence of multiple fluid particles can be modeled. In this regard, the present paper contains the modeling and implementation of the thermal Marangoni stresses, within the framework of the finite-volume/level-set method introduced by Balcázar et al. (2014; 2015a), thus, using the conservative level-set method (Balcázar et al., 2014; Olsson and Kreiss, 2005), mass conservation problem that is known to affect standard level-set formulations (Osher and Sethian, 1988; Sussman and Puckett, 2000) is circumvented. Additionally, the present model is designed in the context of a multiple marker CLS methodology introduced by Balcázar et al. (2015b), which has the ability to solve the interaction of multiple interfaces at the same control volume, allowing for the collision of multiple bubbles or droplets, avoiding the numerical coalescence of the fluid particles.

The present paper is organized as follows: The mathematical formulation is presented in Section 2. Section 3 shows the numerical methods. Model validation and numerical experiments are presented in Section 4. Finally, concluding remarks and future work are discussed in Section 5.

2. Mathematical formulation

2.1. Incompressible two-phase flow and energy equation

The conservation of momentum and mass of two immiscible incompressible and Newtonian fluids are described by the Navier–Stokes equations defined on the spatial domain $\Omega = \Omega_d \cup \Omega_c$ with boundary $\partial\Omega$:

$$\frac{\partial}{\partial t}(\rho_k \mathbf{v}_k) + \nabla \cdot (\rho_k \mathbf{v}_k \mathbf{v}_k) = \nabla \cdot \mathbf{S}_k + \rho_k \mathbf{g} \qquad \text{in } \Omega_k \tag{1}$$

$$\mathbf{S}_k = -p_k \mathbf{I} + \mu_k \left(\nabla \mathbf{v}_k + (\nabla \mathbf{v}_k)^T\right) \tag{2}$$

$$\nabla \cdot \mathbf{v}_k = 0 \qquad \text{in } \Omega_k \tag{3}$$

where subscripts $k = \{d, c\}$ denote the dispersed (d) and continuous (c) fluid phases, $\Gamma = \partial\Omega_d \cap \partial\Omega_c$ is the fluid–fluid interface, ρ and μ denote the density and dynamic viscosity of the fluid phases, $\mathbf{v}$ is the velocity field, $\mathbf{g}$ is the gravity acceleration, p is the pressure, $\mathbf{S}$ is the stress tensor and $\mathbf{I}$ is the identity tensor.

Assuming no mass transfer between the fluid phases yields a continuous velocity condition at the interface:

$$\mathbf{v}_d = \mathbf{v}_c \qquad \text{in } \Gamma \tag{4}$$

The jump in normal stresses along the fluid–fluid interface is balanced by the surface tension. Considering the surface tension coefficient as function of the temperature, $\sigma(T)$, gives the following boundary condition for momentum conservation at the interface:

$$(\mathbf{S}_d - \mathbf{S}_c) \cdot \mathbf{n} = \mathbf{f}_\sigma = \sigma(T)\kappa \mathbf{n} - \nabla_\Gamma \sigma(T) \qquad \text{in } \Gamma \tag{5}$$

where $\mathbf{n}$ is the unit normal vector outward to $\partial\Omega_d$, κ is the interface curvature, and $\nabla_\Gamma = \nabla - \mathbf{n}(\mathbf{n} \cdot \nabla)$ is the tangential surface gradient operator.

The Navier–Stokes equations for the dispersed fluid in $\Omega_d = \Omega_d^1 \cup \ldots \cup \Omega_d^{n_d}$ and continuous fluid in Ω_c, Eqs. (1)–(5), can be combined into a set of equations in Ω, with a singular source term for the surface tension force at the interface $\Gamma = \Gamma_1 \cup \ldots \cup \Gamma_{n_d}$ (Brackbill et al., 1992; Peskin, 1977), defining the superscript n_d as the number of fluid particles in Ω_d:

$$\begin{aligned}\frac{\partial}{\partial t}(\rho \mathbf{v}) + \nabla \cdot (\rho \mathbf{v}\mathbf{v}) \; &= -\nabla p + \nabla \cdot \mu \left(\nabla \mathbf{v} + (\nabla \mathbf{v})^T\right) \\ &\quad + \rho \mathbf{g} + \mathbf{f}_\sigma(T)\delta_\Gamma\end{aligned} \tag{6}$$

$$\nabla \cdot \mathbf{v} = 0 \tag{7}$$

where δ_Γ is the Dirac delta function concentrated at the interface. Since ρ and μ are considered constant in each fluid phase with a jump discontinuity at the interface, they can be defined as:

$$\rho = \rho_d H_d + \rho_c (1 - H_d) \qquad \mu = \mu_d H_d + \mu_c (1 - H_d) \tag{8}$$

with H_d the Heaviside step function that is one in Ω_d and zero elsewhere. At discretized level a continuous treatment of physical properties is adopted in order to avoid numerical instabilities at the interface, according to the CLS method (Balcázar et al., 2014; 2015a; Olsson and Kreiss, 2005).

In order to account for the temperature dependence of surface tension in momentum equation, the temperature distribution must be determined. This requires the solution of the energy equations in the two fluid phases. If the contribution of viscous dissipation is ignored, and heat sources or sinks are not present, these equations can be written as

$$\frac{\partial T_k}{\partial t} + \nabla \cdot (\mathbf{v}_k T_k) = \frac{1}{\rho_k c_{p,k}} \nabla \cdot (\lambda_k \nabla T_k) \qquad \text{in } \Omega_k \tag{9}$$

Please cite this article as: N. Balcázar et al., A level-set model for thermocapillary motion of deformable fluid particles, International Journal of Heat and Fluid Flow (2016), http://dx.doi.org/10.1016/j.ijheatfluidflow.2016.09.015

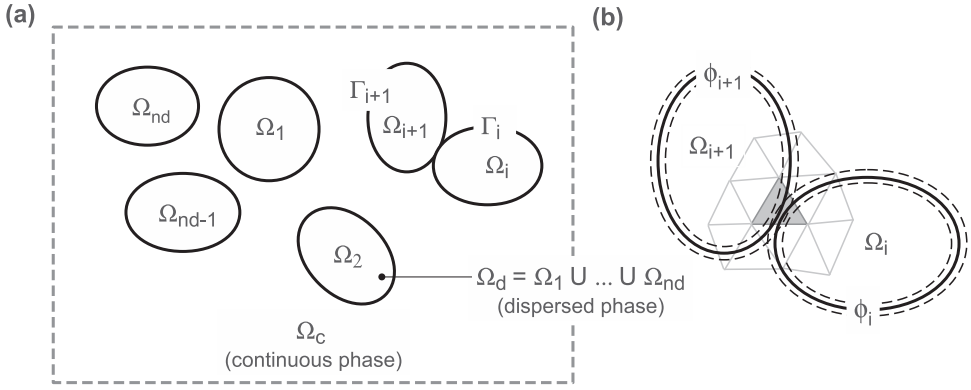

Fig. 1. (a) Fluid–fluid interfaces $\Gamma_1, \ldots, \Gamma_{n_d}$ captured by multiple level-set functions $\phi_1, \ldots, \phi_{n_d}$, where $\Gamma_i = \{\mathbf{x} | \phi_i(\mathbf{x}, t) = 0.5\}$. (b) Level-set functions (markers) ϕ_i and ϕ_{i+1} on the same control volume.

with heat capacity c_p and thermal conductivity λ. These physical properties are assumed to be constant at each fluid phase. Furthermore, the temperature is considered to be continuous at the interface,

$$T_d = T_c \qquad \text{in } \Gamma \tag{10}$$

Assuming no phase change, the energy balance at the interface yields the continuity of heat flux

$$(\lambda_d \nabla T_d - \lambda_c \nabla T_c) \cdot \mathbf{n} = 0 \qquad \text{in } \Gamma \tag{11}$$

Thus, Eqs. (9)–(11) can be written in Ω as

$$\frac{\partial T}{\partial t} + \nabla \cdot (\mathbf{v}T) = \frac{1}{\rho c_p} \nabla \cdot (\lambda \nabla T) \qquad \text{in } \Omega \tag{12}$$

with λ and c_p defined as

$$\lambda = \lambda_d H_d + \lambda_c (1 - H_d) \qquad c_p = c_{p,d} H_d + c_{p,c} (1 - H_d) \tag{13}$$

At discretized level, thermal properties, λ and c_p, will be regularized in the context of the CLS method, according to the Section 2.4.

2.2. Interface capturing and multiple marker level-set method

The two major challenges of simulating interfaces between different fluids are to maintain a sharp front and to compute the surface tension accurately (Tryggvason et al., 2001). Regarding the first issue, the CLS method introduced in Balcázar et al. (2014) is used for interface capturing. Moreover, in order to avoid the numerical coalescence of the fluid–fluid interfaces, a multiple marker level-set method introduced in Balcázar et al. (2015a) is used to follow the motion of each fluid particle at the dispersed phase. Therefore, different level-set functions (markers), $\phi_1, \ldots, \phi_{n_d}$, can be captured in the same control volume, allowing for the collision of the fluid particles, as illustrated in Fig. 1a–b.

In the CLS method (Balcázar et al., 2014; Olsson and Kreiss, 2005) the interface is implicitly represented by the 0.5 isosurface of the regularized indicator function ϕ_i:

$$\phi_i(\mathbf{x}, t) = \frac{1}{2}\left(tanh\left(\frac{d_i(\mathbf{x}, t)}{2\varepsilon}\right) + 1\right), \quad i = 1, \ldots, n_d \tag{14}$$

where d_i is the signed distance function associated to the ith fluid particle, and ε a parameter that sets the thickness of the profile. Eq. (14) is used to initialize the CLS functions ϕ_i, from the distance function d_i generated for each fluid–fluid interface. Moreover, the ith interface transport equation can be written in conservative form provided the velocity field is solenoidal, $\nabla \cdot \mathbf{v} = 0$, namely,

$$\frac{\partial \phi_i}{\partial t} + \nabla \cdot \phi_i \mathbf{v} = 0, i = 1, 2, \ldots, n_d \tag{15}$$

Furthermore, an additional re-initialization equation is introduced in order to keep a sharp and constant interface profile

$$\frac{\partial \phi_i}{\partial \tau} + \nabla \cdot \phi_i (1 - \phi_i) \mathbf{n}_i = \nabla \cdot \varepsilon \nabla \phi_i, i = 1, 2, \ldots, n_d \tag{16}$$

This equation is advanced in pseudo-time τ, it consists of a compressive term, $\phi_i(1 - \phi_i)\mathbf{n}_i|_{\tau=0}$, which forces the level-set function to be compressed onto the interface along the normal vector $\mathbf{n}_i$, and of a diffusion term $\nabla \cdot \varepsilon \nabla \phi_i$ that ensure the profile remains of characteristic thickness $\varepsilon = 0.5h^{0.9}$, with h defined as the grid size (Balcázar et al., 2014).

2.3. Surface tension

Implementing surface tension in a numerical scheme involves two issues: the curvature κ needs to be determined and the resulting pressure jump must be applied appropriately to the fluids. Because a finite-volume approach is used for discretization of the governing equations, the aforementioned problems can be conveniently addressed by means of the continuous surface force (CSF) model (Brackbill et al., 1992), which is adapted to the multiple-marker/level-set method introduced by Balcázar et al. (2015a), and extended to take into account the temperature dependence of surface tension

$$\begin{aligned} \mathbf{f}_\sigma \delta_\Gamma &= \sum_{i=1}^{n_d} \mathbf{f}_{\sigma,i} \delta_{\Gamma_i} \\ &= \sum_{i=1}^{n_d} (\sigma(T) \kappa_i(\phi_i) \mathbf{n}_i - \nabla \sigma(T) + \mathbf{n}_i (\mathbf{n}_i \cdot \nabla) \sigma(T)) \parallel \nabla \phi_i \parallel \end{aligned} \tag{17}$$

where $\kappa_i(\phi_i)$ and $\mathbf{n}_i$ are given by

$$\mathbf{n}_i(\phi_i) = \frac{\nabla \phi_i}{\|\nabla \phi_i\|} \qquad \kappa_i(\phi_i) = -\nabla \cdot \mathbf{n}_i, i = 1, 2, \ldots, n_d \tag{18}$$

To obtain a cell averaged value, the curvature is integrated over each finite volume Ω_P:

$$\kappa_{i,P} = -\frac{1}{V_P} \int_{\Omega_P} \nabla \cdot \mathbf{n}_i dV \tag{19}$$

Applying the Gauss theorem yields

$$\kappa_{i,P} = -\frac{1}{V_P} \int_{S_P} \mathbf{n}_i \cdot d\mathbf{A} \tag{20}$$

Here $\nabla \phi_i$ is calculated by means of the least-squares method (Balcázar et al., 2014; Kothe et al., 1996), $\mathbf{A}$ is the area vector, V_P is the volume, S_P is the surface of Ω_P, and the subindex P denote the Pth control volume. Further details on the application of the least

Please cite this article as: N. Balcázar et al., A level-set model for thermocapillary motion of deformable fluid particles, International Journal of Heat and Fluid Flow (2016), http://dx.doi.org/10.1016/j.ijheatfluidflow.2016.09.015

squares method for gradient evaluation are given in Balcázar et al. (2014).

The surface tension coefficient is taken to be a linearly decreasing function of the temperature

$$\sigma = \sigma_0 - \sigma_T(T - T_0) \tag{21}$$

where $\sigma_T = -d\sigma/dT = constant$, σ_0 is the surface tension at the reference temperature T_0. In general, the coefficient σ_T is positive and it depends of the temperature, however, a constant σ_T provides a very good approximation for most fluids in a range of small temperature variation. This model can be extended to other equations of state.

2.4. Regularization of physical properties

Finally, fluid properties are regularized by means of a global level-set function, according to the multiple-marker/level-set method (Balcázar et al., 2015a):

$$\phi_d(\mathbf{x}, t) = max\{\phi_1(\mathbf{x}, t), \ldots, \phi_{n_d-1}(\mathbf{x}, t), \phi_{n_d}(\mathbf{x}, t)\} \tag{22}$$

Thus, physical properties are computed at the discretized level as follow

$$\rho = \rho_d\phi_d + \rho_c(1 - \phi_d) \tag{23}$$

$$\mu^{-1} = \mu_d^{-1}\phi_d + \mu_c^{-1}(1 - \phi_d) \tag{24}$$

$$\rho c_p = \rho_d c_{p,d}\phi_d + \rho_c c_{p,c}(1 - \phi_d) \tag{25}$$

$$\lambda^{-1} = \lambda_d^{-1}\phi_d + \lambda_c^{-1}(1 - \phi_d) \tag{26}$$

All physical properties of the respective phases are assumed to be constant, moreover the local average dynamic viscosity and thermal conductivity are calculated via harmonic averaging (Deen and Kuipers, 2013; Patankar, 1980; Prosperetti, 2002).

3. Numerical method

The numerical algorithms presented in this paper are designed in the context of the unstructured finite-volume/level-set method introduced by Balcázar et al. (2014; 2015a). Thus, the Navier–Stokes equations, Eq. (6), energy equation, Eq. (12), and interface capturing equations, Eqs. (15)–(16), are solved with a finite-volume discretization of the physical domain on a collocated unstructured mesh, where both scalar and vector variables (p, $\mathbf{v}$, T and ϕ) are stored in the cell centroids. Furthermore, the convective term of momentum Eq. (6), energy Eq. (12) and interface transport Eq. (15) is explicitly computed approximating the fluxes at cell faces with a TVD-Superbee limiter scheme (Balcázar et al., 2014; Sweby, 1984) (see Appendix A). Diffusive terms are centrally differenced, whereas a distance-weighted linear interpolation is used to find the cell face values of physical properties and interface normals. Gradients are computed at cell centroids by means of the least-squares method (Balcázar et al., 2014). Regarding the re-initialization Eq. (16), a central difference scheme is used to discretize both convective and diffusive terms. The resolution of the velocity and pressure fields is achieved by a standard fractional step projection method (Chorin, 1968). Thus, the global algorithm for thermal two-phase flows with variable surface tension is summarized as follows:

1. Initialize $\mathbf{v}(\mathbf{x}_P, 0)$, $\phi_i(\mathbf{x}_P, 0)$, $T(\mathbf{x}_P, 0)$ physical properties and interface geometric properties.
2. The time-step, Δt, which is limited by the CFL conditions and the stability condition for the capillary force defined by Brackbill et al. (1992), is calculated as
$$\Delta t = C_t min\left(\frac{h}{||\mathbf{v}||}, \frac{\rho h^2}{\mu}, \left(\frac{h}{||\mathbf{g}||}\right)^{1/2}, h^{3/2}\left(\frac{\rho_1 + \rho_2}{4\pi\sigma}\right)^{1/2}\right) \tag{27}$$
where $C_t = 0.1$ unless otherwise stated. Recently, Denner and van Wachem (2015a) have reported a revised capillary time-step constraint, derived from numerical stability and signal processing theory. In the present work, the minimum time-step calculated according to Eq. (27), is multiplied by the coefficient $C_t = 0.1$, which results in a robust numerical solution for the simulations reported in this research.
3. The fluid–fluid interfaces are advected by means of the CLS method introduced by Balcázar et al. (2014; 2015a). Advection Eq. (15) and re-initialization Eq. (16) are explicitly integrated in time with a 3-step third-order accurate TVD Runge-Kutta method (Gottlieb and Chi-Wang, 1998). Moreover, solving re-initialization Eq. (16) to steady-state results in a smooth transition of ϕ_i at the interface that depends of the diffusion coefficient $\varepsilon = 0.5h^{0.9}$, where h is the grid size (Balcázar et al., 2014). This configuration leads to an interface thickness, with a distance between contours of $\phi = 0.1$ and $\phi = 0.9$, of around three times the grid size (Balcázar et al., 2014). Furthermore, ε is chosen as small as possible in order to keep a sharp representation of the interface, while numerical stability of Eq. (16) is not affected. In present simulations one iteration per physical time step of re-initialization Eq. (16) was sufficient to keep the profile of the CLS functions. The reader is referred to the work of Balcázar et al. (2014; 2015a) for technical details on the multiple marker CLS method.
4. The temperature field, T^{n+1}, is calculated using an explicit Euler scheme
$$\frac{T^{n+1} - T^n}{\Delta t} = -\mathbf{A}_h^T(T^n) + \frac{1}{\rho c_p}\mathbf{D}_h^T(T^n) \tag{28}$$
where $D_h^T(T) = \nabla_h \cdot (\lambda \nabla_h T)$ represents the diffusion operator, $\mathbf{A}_h^T(T) = \nabla_h \cdot (\mathbf{v}T)$ is the convective operator, and ∇_h represents the gradient operator.
5. Physical properties (ρ, μ, λ, c_p) are updated at each control volume, according to the Section 2.4, whereas surface tension coefficient, $\sigma(T)$, is calculated by Eq. (21).
6. The fractional-step method (Chorin, 1968) is used to solve the pressure-velocity coupling. Indeed, a predictor velocity $\mathbf{v}^*$ is evaluated by
$$\frac{\rho\mathbf{v}^* - \rho^n\mathbf{v}^n}{\Delta t} = -\frac{3}{2}\mathbf{A}_h^{\mathbf{v}}(\rho\mathbf{v}^n) + \frac{1}{2}\mathbf{A}_h^{\mathbf{v}}\left(\rho\mathbf{v}^{n-1}\right) + \mathbf{D}_h^{\mathbf{v}}(\mathbf{v}^n) + \rho\mathbf{g} + \sum_{i=1}^{n_d}(\sigma(T)\kappa_i(\phi_i)\mathbf{n}_i - \nabla_h\sigma(T) + \mathbf{n}_i(\mathbf{n}_i \cdot \nabla_h)\sigma(T))||\nabla_h\phi_i|| \tag{29}$$
where $D_h^{\mathbf{v}}(\mathbf{v}) = \nabla_h \cdot \mu(\nabla_h\mathbf{v} + (\nabla_h\mathbf{v})^T)$ is the diffusion operator, and $\mathbf{A}_h^{\mathbf{v}}(\rho\mathbf{v}) = \nabla_h \cdot (\rho\mathbf{v}\mathbf{v})$ is the convective operator. Moreover, an explicit Adams-Bashforth scheme has been used for the temporal discretization of the convective term, $\nabla_h\sigma$ is evaluated by means of the least-squares method (Balcázar et al., 2014), whereas $\mathbf{n}_i$ and κ_i are calculated at each control volume according to Eq. (18).
7. Substituting Eq. (31) into the Eq. (7) yields a Poisson equation for pressure field
$$\nabla_h \cdot \left(\frac{1}{\rho}\nabla_h(p^{n+1})\right) = \frac{1}{\Delta t}\nabla_h \cdot (\mathbf{v}^*) \tag{30}$$
Discretization of Eq. (30) leads to a linear system, which is solved by means of a preconditioned conjugate gradient method.

Please cite this article as: N. Balcázar et al., A level-set model for thermocapillary motion of deformable fluid particles, International Journal of Heat and Fluid Flow (2016), http://dx.doi.org/10.1016/j.ijheatfluidflow.2016.09.015

8. The resulting velocity $\mathbf{v}^*$ from Eq. (29), does not satisfy the incompressibility constraint, Eq. (7). Thus, a corrected velocity field is obtained according to the fractional-step method (Chorin, 1968)

$$\mathbf{v}^{n+1} = \mathbf{v}^* - \frac{\Delta t}{\rho}\nabla_h(p^{n+1}) \tag{31}$$

9. In order to avoid pressure-velocity decoupling when the pressure projection is made on collocated meshes (Felten and Lund, 2006; Rhie and Chow, 1983), a cell face velocity $\mathbf{v}_f$ is calculated so that $\nabla_h \cdot \mathbf{v} = 0$ at each control volume (Balcázar et al., 2014). Namely in discretized form:

$$\mathbf{v}_f = \sum_{q\in\{P,F\}} \frac{1}{2}\left(\mathbf{v}_q^{n+1} + \frac{\Delta t}{\rho(\phi_q)}(\nabla_h p^{n+1})_q\right) - \frac{\Delta t}{\rho_f}(\nabla_h p^{n+1})_f \tag{32}$$

where P and F are denoting the adjacent cell nodes with a common face f. The reader is referred to Appendix B or the work introduced by Balcázar et al. (2014) for further details on the origin of Eq. (32). This cell-face velocity is used to advect the CLS function in Eq. (15), momentum in Eq. (6) and temperature in Eq. (12).

10. Repeat steps 2–9 until time step required.

The numerical methods introduced in this work have been implemented in the framework of a parallel C++/MPI code called TermoFluids (Lehmkuhl et al., 2007). The code is run on the supercomputer MareNostrum III using 128 cores for 3D simulations of single droplets (Section 4.2), up to 512 processors for 3D simulations of multiple droplets (Section 4.3). The reader is referred to the work of Balcázar et al. (2014) for additional technical details on the finite-volume discretization of the general convection-diffusion equation on unstructured meshes, including the Navier–Stokes and CLS equations. Furthermore, verification and validation of the numerical methods for isothermal two-phase flows with constant surface tension have been reported in Balcázar et al. (2014, 2016, 2015a, 2015b).

4. Model validation and numerical experiments

A first test case is presented in Appendix C, in order to validate the present numerical methods in the context of thermal two-phase flow with constant surface tension. Next sections are devoted to the verification and validation of the proposed level-set model in thermocapillary flows, including the thermocapillary driven convection of two superimposed planar fluids at small Reynolds and Marangoni numbers, thermocapillary migration of single fluid particles, and simulation of thermocapillary motion and interaction of multiple fluid particles.

The dimensionless parameters controlling the thermocapillary flow are the Marangoni number (Ma), Reynolds number (Re), Capillary number (Ca) and the ratios of physical properties ($\eta_\rho, \eta_\mu, \eta_\lambda, \eta_{c_p}$), defined as follow

$$Ma = \frac{U_r L_r \rho_c c_{p,c}}{\lambda_c}; \qquad Re = \frac{U_r L_r \rho_c}{\mu_c}; \qquad Ca = \frac{U_r \mu_c}{\sigma_0} \tag{33}$$

$$\eta_\rho = \frac{\rho_d}{\rho_c}; \qquad \eta_\mu = \frac{\mu_d}{\mu_c}; \qquad \eta_\lambda = \frac{\lambda_d}{\lambda_c}; \qquad \eta_{c_p} = \frac{c_{p,d}}{c_{p,c}} \tag{34}$$

where the subindex c refers to the continuous phase, the subindex d refers to the dispersed phase, L_r and U_r are the characteristic length and velocity of the system, respectively. These characteristic dimensions (L_r, U_r) will be defined if necessary according to each test case introduced in next sections. The effect of gravity is neglected, $\mathbf{g} = \mathbf{0}$, and phase change is not taken into account.

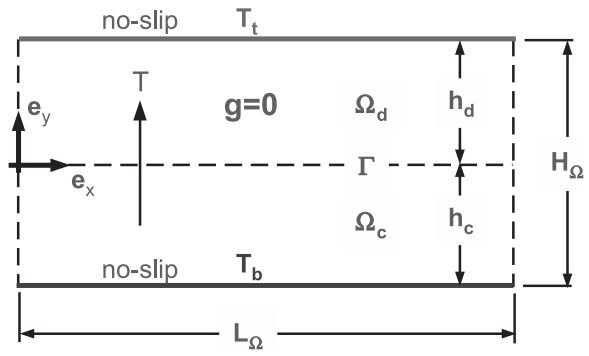

Fig. 2. Computational set-up in thermocapillary convection of two superimposed planar fluids.

4.1. Thermocapillary convection of two superimposed planar fluids

The computational domain is illustrated in Fig. 2 with $-0.5L_\Omega \leqslant x \leqslant 0.5L_\Omega$, $-h_c \leqslant y \leqslant h_d$, $L_\Omega = 4H_\Omega$, and the interface Γ located at $y = 0$. The periodic boundary conditions are applied in the x direction, no-slip conditions are imposed on the upper and lower walls, whereas the wall temperatures are specified as $T(x, h_d) = T_t$ on the top boundary and a sinusoidal temperature on the lower wall at $y = -h_c$

$$T(x, -h_c) = T_b + \Delta T_b cos(kx) \tag{35}$$

with $T_b > T_t$, and $k = 2\pi/L_\Omega$ defined as the wave number. The characteristic scales of length and velocity are $L_r = h_c$ and $U_r = \sigma_T \Delta T_b h_c/(L_\Omega \mu_c)$, respectively. Therefore the dimensionless numbers defined in Eq. (33) can be written as

$$Ma = \frac{\sigma_T\ \triangle T_b\ h_c^2\ \rho_c\ c_{p,c}}{L_\Omega\ \mu_c\ \lambda_c};\quad Re = \frac{\sigma_T\ \triangle T_b\ h_c^2\ \rho_c}{L_\Omega\ \mu_c^2};\quad Ca = \frac{\sigma_T\ \triangle T_b\ h_c}{L_\Omega\ \sigma_0} \tag{36}$$

When $Re \ll 1$, $Ma \ll 1$, and $Ca \ll 1$, the convective transport of momentum and energy are negligible, and the interface remains plane. The analytical solutions for the stream function $\psi(x, y)$ and temperature field $T(x, y)$ were obtained by Pendse and Esmaeeli (2010) as follows

$$\psi(x,y) = (U_{max}/k)\left(\sin h^2(\alpha) - \alpha^2\right)^{-1}\sin(kx)\Big(ky\ \sin h^2(\alpha)\ldots$$
$$cosh(ky) - (1/2)\left(2\alpha^2 + ky(sinh(2\alpha) - 2\alpha)sinh(ky)\right)\Big) \tag{37}$$

$$T(x,y) = \frac{(T_t - T_b)y + \eta_\lambda T_t h_c + T_b h_d}{h_d + \eta_\lambda h_c} + \Delta T_b\ f(\alpha,\beta,\eta_\lambda)\ sinh(\alpha - ky)cos(kx) \tag{38}$$

for the fluid in Ω_d, and

$$\psi(x,y) = (U_{max}/k)\left(\sin h^2(\beta) - \beta^2\right)^{-1}\sin(kx)\Big(ky\ \sin h^2(\beta)\ldots$$
$$cosh(ky) - (1/2)\left(2\beta^2 - ky(sinh(2\beta) - 2\beta)sinh(ky)\right)\Big) \tag{39}$$

$$T(x,y) = \frac{\eta_\lambda(T_t - T_b)y + \eta_\lambda h_c + T_c h_d}{h_d + \eta_\lambda h_c} + \Delta T_b cos(kx)\ldots$$
$$f(\alpha,\beta,\eta_\lambda)(sinh(\alpha)cosh(ky) - \eta_\lambda sinh(ky)cosh(\alpha)) \tag{40}$$

for the fluid in Ω_c. The parameters in the aforementioned equations are defined as

$$\alpha = h_d k;\ \beta = h_c k \tag{41}$$

$$f(\alpha,\beta,\eta_\lambda) = \frac{1}{\eta_\lambda sinh(\beta)cosh(\alpha) + sinh(\alpha)cosh(\beta)} \tag{42}$$

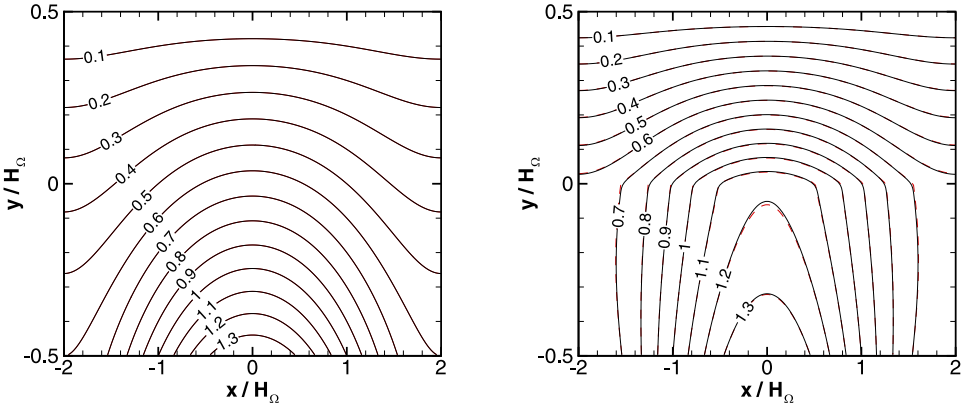

Fig. 3. Thermocapillary convection of two superimposed planar fluids. Temperature contours for $\eta_\lambda = 1$ (left) and $\eta_\lambda = 0.1$ (right). Analytical (red line) and numerical (black line) results, $h = H_\Omega/120$. (For interpretation of the references to color in this figure legend, the reader is referred to the web version of this article.)

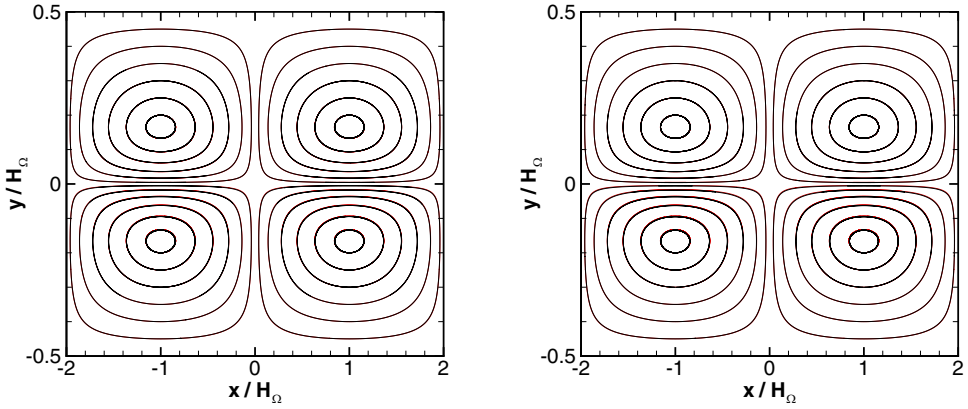

Fig. 4. Thermocapillary convection of two superimposed planar fluids. Streamline contours for $\eta_\lambda = 1$ (left) and $\eta_\lambda = 0.1$ (right). Analytical (red line) and numerical (black line) results, $h = H_\Omega/120$. (For interpretation of the references to color in this figure legend, the reader is referred to the web version of this article.)

and

$$U_{max} = -\left(\frac{\Delta T_b \sigma_T c_{p,c}}{\lambda_c}\right) g(\alpha, \beta, \eta_\lambda) h(\alpha, \beta, \eta_\mu) \tag{43}$$

where

$$g(\alpha, \beta, \eta_\lambda) = f(\alpha, \beta, \eta_\lambda) sinh(\alpha) \tag{44}$$

$$\begin{aligned} h(\alpha, \beta, \eta_\mu) &= \left(\sin h^2(\alpha) - \alpha^2\right)\left(\sin h^2(\beta) - \beta^2\right)... \\ &\left(\eta_\mu \left(\sin h^2(\beta) - \beta^2\right)(sinh(2\alpha) - 2\alpha)\right. \\ &+\left(\sin h^2(\alpha) - \alpha^2\right)\left(\sin h^2(\alpha) - \alpha^2\right)\left(\sin h(2\beta) - 2\beta\right)\Big)^{-1} \end{aligned} \tag{45}$$

In addition the velocity field can be obtained from $\psi(x, y)$ by taking $\mathbf{v} \cdot \mathbf{e}_x = \partial\psi/\partial y$ and $\mathbf{v} \cdot \mathbf{e}_y = -\partial\psi/\partial x$ (Fig. 5).

Present simulations are performed on a uniform cartesian mesh of $\{160 \times 40,\ 320 \times 80,\ 480 \times 120\}$ grid points with $h = \{H_\Omega/40, H_\Omega/80, H_\Omega/120\}$, respectively. The dimensionless parameters are $Re = 0.01$, $Ma = 0.01$, $Ca = 0.01$, whereas the ratio of physical properties are set to unity, $\eta_\rho = 1$, $\eta_\mu = 1$, $\eta_{c_p} = 1$, except for thermal conductivity ratio which takes the values $\eta_\lambda = \{1, 0.1\}$. Since $Re \ll 1$, $Ma \ll 1$, and $Ca \ll 1$, present cases correspond to the creeping flow regime, indeed, the density ratio does not play a role. Furthermore, since the simulations are carried out for steady state, the results do not depend of the heat capacity ratio η_{c_p}.

The contours of stream function and temperature field are shown in Figs. 3 and 4, for thermal conductivity ratio $\eta_\lambda = 1$ and $\eta_\lambda = 0.1$, respectively, using a grid size $h = H_\Omega/120$. Fig. 6 shows a further comparison between present simulations against analytical results for T and $\mathbf{v} \cdot \mathbf{e}_y$ on the line $x/H_\Omega = 0$. From the aforementioned results, it can be concluded that present simulations are in excellent agreement with analytical solutions given by Eqs. (37)–(40). Additionally, in order to demonstrate the grid convergence of the present model, Table 1 shows the E_1^ϕ norms of the differences between the analytical results (ϕ_i^{exact}) and numerical solutions (ϕ_i^{num}), defined as $E_1^\phi = (1/N_{cv}) \sum_i^{N_{cv}} ||\phi_i^{num} - \phi_i^{exact}||$, where N_{cv} is the number of control volumes in Ω. It is observed that as the grid size (h) decreases, the E_1^ϕ norm decreases for both velocity field ($\phi = \{v_x, v_y\}$) and temperature field ($\phi = T$). We also note that differences E_1^T are slighter higher for the cases with $\eta_\lambda = 0.1$ in comparison with $\eta_\lambda = 1$, which can be explained by the jump in thermal conductivity at the interface when $\eta_\lambda \neq 1$.

Fig. 3 illustrates the contours of temperature field for $\eta_\lambda = \{1, 0.1\}$. It is observed, that for the case with $\eta_\lambda = 1$ the temperature contours present equal slopes at the fluid–fluid interfacial zone, whereas, for $\eta_\lambda = 0.1$ the temperature contours at the interface are different at both fluid regions, reflecting the fact that the ratio of the thermal conductivities of the fluids plays an important role in the strengthens of the thermocapillary convection. Moreover, the cosine function used as boundary condition for the temperature at the bottom wall leads to non-uniform distribution of temperature at the interface. Indeed, the fluids are set in motion by the action of a shear force originated by the temperature gradient at the interface, and directed from the symmetry axis $x/H_\Omega = 0$ toward both sides in Ω, as is illustrated by streamlines in Fig. 3. Furthermore, Fig 4 shows that the fluid flow consist of

Please cite this article as: N. Balcázar et al., A level-set model for thermocapillary motion of deformable fluid particles, International Journal of Heat and Fluid Flow (2016), http://dx.doi.org/10.1016/j.ijheatfluidflow.2016.09.015

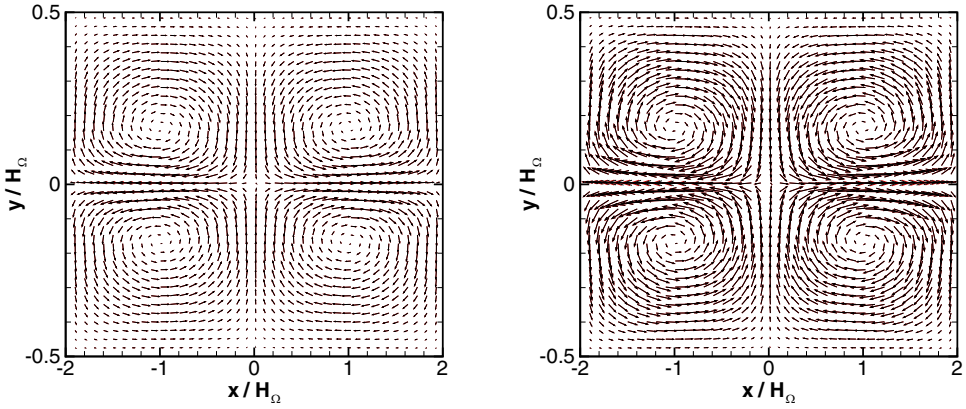

Fig. 5. Thermocapillary convection of two superimposed planar fluids. Velocity vectors for $\eta_\lambda = 1$ (left) and $\eta_\lambda = 0.1$ (right). Analytical (red line) and numerical (black line) results, $h = H_\Omega/120$. (For interpretation of the references to color in this figure legend, the reader is referred to the web version of this article.)

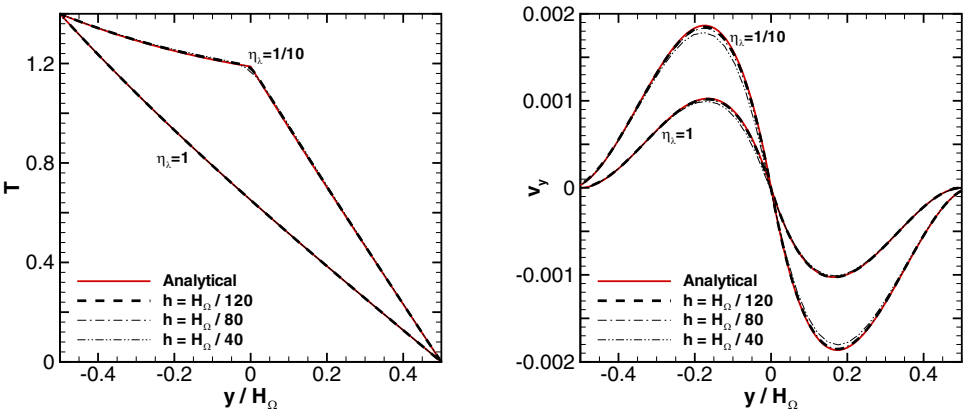

Fig. 6. Velocity ($v_y = \mathbf{v} \cdot \mathbf{e}_y$) and temperature ($T$) profiles at $x/H_\Omega = 0$, for thermocapillary convection of two superimposed planar fluids $\eta_\lambda = \{1.0, 1/10\}$.

Table 1
Relative differences between the analytical solutions and the numerical results for Section 4.1. $E_1^\phi = (1/N_{cv}) \sum_i^{N_{cv}} ||\phi_i^{num} - \phi_i^{exact}||$, where N_{cv} is the number of control volumes, and $\phi = \{v_x, v_y, T\}$.

	$\eta_\lambda = 1$			$\eta_\lambda = 0.1$		
h	E_1^T	$E_1^{v_x}$	$E_1^{v_y}$	E_1^T	$E_1^{v_x}$	$E_1^{v_y}$
$H_\Omega/40$	1.8×10^{-5}	8.5×10^{-5}	1.2×10^{-5}	3.1×10^{-3}	1.7×10^{-4}	2.6×10^{-5}
$H_\Omega/80$	9.2×10^{-6}	2.8×10^{-5}	3.9×10^{-6}	1.6×10^{-3}	5.7×10^{-5}	9.0×10^{-6}
$H_\Omega/120$	8.5×10^{-6}	1.4×10^{-5}	1.6×10^{-6}	9.6×10^{-4}	3.0×10^{-5}	5.3×10^{-6}

4 regions with counter-rotating vortices, where the sense of fluid circulation is given by the temperature gradient at the interface. Since the domain is periodic in the x direction, the velocities decrease as they approach to the left and right boundaries, therefore, the fluids are also forced to move upward in Ω_d, or downward in Ω_c, which explain the circulation patterns illustrated in Figs. 3 and 4. Thus, present results are consistent with analytical solutions of Pendse and Esmaeeli (2010), and with recent simulations reported by Liu et al. (2012), Zheng et al. (2016), Guo and Lin (2015), where the same problem was researched numerically by means of lattice Boltzmann and phase field methods.

4.2. Thermocapillary motion of single fluid particles

Next sections are devoted to the simulation of Marangoni migration of single and multiple fluid particles. The characteristic scales of length, velocity and temperature are denoted by $L_r = d/2$, $U_r = \sigma_T ||\nabla T_\infty|| (d/2)/\mu_c$ and $T_r = (d/2)||\nabla T_\infty||$, respectively. Therefore, the dimensionless parameters defined in Eq. (33) are written as follow

$$Ma = \frac{\sigma_T \parallel \nabla T_\infty \parallel d^2 \rho_c c_{p,c}}{4\mu_c \lambda_c}; \qquad Re = \frac{\sigma_T \parallel \nabla T_\infty \parallel d^2 \rho_c}{4\mu_c^2}; \qquad Ca = \frac{\sigma_T \parallel \nabla T_\infty \parallel d}{2\sigma_0} \tag{46}$$

where the subindex c refers to the continuous phase, the subindex d refers to the drop fluid phase, U_r is the named thermocapillary velocity, d is the initial droplet diameter, $||\nabla T_\infty||$ is the temperature gradient imposed in the continuous fluid, whereas the ratios of physical properties are defined by Eq. (34). Additionally, the dimensionless velocity, $V^* = (\mathbf{e}_y \cdot \mathbf{v}_c)/U_r$ with $\mathbf{v}_c = \int_\Omega \phi \mathbf{v} dV / \int_\Omega \phi dV$, and dimensionless time, $t^* = 2tU_r/d$, are used to express the numerical results.

The fluids are initially at rest without gravity and the temperature linearly increases from the cold bottom wall toward the hot top wall

$$T(x, y, z) = T_b + \frac{T_t - T_b}{H_\Omega} y = T_b + ||\nabla T_\infty|| y \tag{47}$$

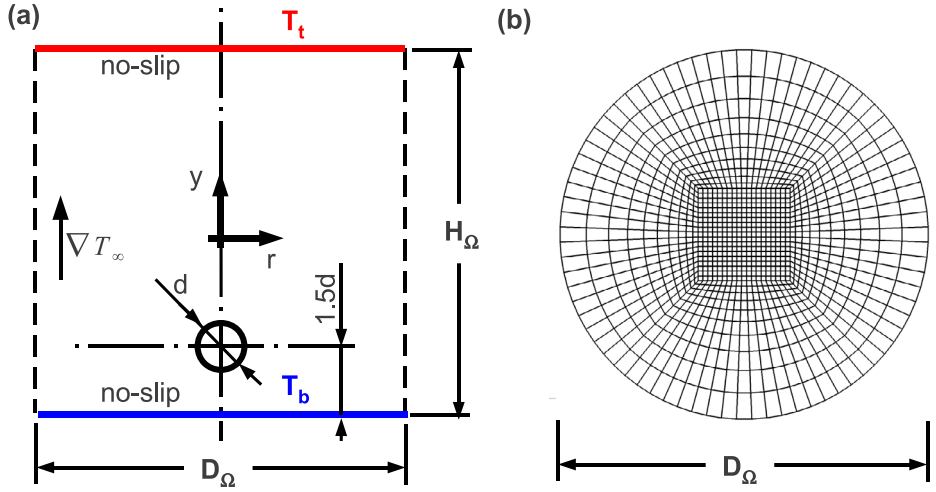

Fig. 7. (a) Schematic diagram of the spatial domain. (b) Cross section of the mesh, plane perpendicular to the symmetry axis y.

Table 2
Mesh parameters used in 3D simulations of thermocapillary motion of isolated fluid particles. Here N_{planes} is the number of planes in which the symmetry axis of Ω is divided.

Mesh	(D_Ω, H_Ω)	Cells	*Cells/plane*	N_{planes}	Cell geometry	h
M1	$(8d, 8d)$	9.40×10^5	4700	200	hexahedral	$d/25$
M2	$(8d, 8d)$	1.79×10^6	7440	240	hexahedral	$d/30$
M3	$(8d, 8d)$	2.78×10^6	9940	280	hexahedral	$d/35$
M4	$(8d, 8d)$	4.09×10^6	12800	320	hexahedral	$d/40$

with T_t the temperature of the top wall and T_b the temperature of the bottom wall. The computational setup is illustrated in Fig. 7a, whereas a cross section of mesh used for 3D simulations is presented in Fig. 7b.

4.2.1. Thermocapillary migration in the limit of zero Marangoni number

In the limit of zero Marangoni number and small Reynolds number, Young et al. (1959) derived the named YGB theory for the prediction of the steady state migration velocity (U_{YGB}) of a drop in an infinite domain with constant temperature gradient field, $||\nabla T_\infty||$, such that the convective transport of momentum and energy are negligible

$$\frac{U_{YGB}}{U_r} = \frac{2}{(2+3\mu_d/\mu_c)(2+\lambda_d/\lambda_c)} \tag{48}$$

where all the physical properties are assumed to be constant except for the surface tension, which is assumed to vary linearly with temperature.

In present simulations, a 3D cylindrical domain Ω of diameter $D_\Omega = 8d$ and height $H_\Omega = 8d$ is considered, as shown Fig. 7. Ω is divided by hexahedral control volumes generated by a constant step extrusion $h = H_\Omega/N_{planes}$, of a two-dimensional unstructured grid of quadrilateral cells along the symmetry axis of Ω, as is summarized in Table 2. In order to maximize the droplet resolution, the mesh was concentrated around the symmetry axis of Ω using a constant grid size, h, which grows exponentially to the border where it reaches a maximum size, as Fig. 7b illustrates. A spherical drop of diameter d is placed on the symmetry axis of Ω, at 1.5d above the bottom wall. No-slip boundary conditions are applied on the top and bottom walls, and Neumann boundary condition is used on the lateral wall.

Table 3 shows the nondimensional parameters used in present simulations. In addition, the theoretical migration velocity of a spherical drop, U_{YGB}/U_r, is also included. Fig. 8 shows the temporal evolution of the dimensionless migration velocity, V^*, versus dimensionless time, t^*, using the present method with different grid resolutions. The influence of the grid size, h, is summarized in Table 4. It is found that the difference in the calculated migration velocities is no more than 1% between the meshes with $h = d/35$ and $h = d/40$, therefore the finest mesh resolution $h = d/35$ is selected for discussion of further numerical results unless otherwise stated.

Table 3
Dimensionless parameters used in simulations, and the corresponding theoretical migration velocity (U_{YGB}).

Case	*Re*	*Ca*	*Ma*	η_ρ	η_μ	η_λ	η_{c_p}	U_{YGB}/U_r
A	$0.06\bar{6}$	$0.06\bar{6}$	$0.06\bar{6}$	1.0	1.0	1.0	1.0	$0.13\bar{3}$
B	0.01	0.01	$0.016\bar{6}$	0.5	0.5	0.5	0.5	0.228

Table 4
Grid convergence of the migration velocity, $\varepsilon_r = |(V^* - V^*_{h=d/40})/V^*_{h=d/40}|$. Case A: $Re = Ma = Ca = 0.06\bar{6}$, $\eta_\rho = \eta_\mu = \eta_{c_p} = \eta_\lambda = 1.0$. Case B: $Re = Ma = 0.01$, $Ca = 0.016\bar{6}$, $\eta_\rho = \eta_\mu = \eta_{c_p} = \eta_\lambda = 0.5$.

Mesh	h	Case A		Case B	
		V^*	ε_r	V^*	ε_r
M_1	$d/25$	0.1241	1.9%	0.1946	7.9%
M_2	$d/30$	0.1259	1.5%	0.2057	2.6%
M_3	$d/35$	0.1271	0.9%	0.2088	1.1%
M_4	$d/40$	0.1278	–	0.2112	–

Fig. 8a shows that the present level-set model converges to an asymptotic value $V^*/U_{YGB} = 0.93$ for Case A, which is consistent with the data reported by Maa and Bothe (2011) and Nas and Tryggvason (2003). Fig. 8b shows also an asymptotic convergence to the value $V^*/U_{YGB} = 0.96$ which is comparable to the value 0.96 reported in Brady et al. (2011) using a level-set model, and the value 0.97 calculated by Muradoglu and Tryggvason (2008) using the front-tracking method. The slower rise velocities in the finite

Please cite this article as: N. Balcázar et al., A level-set model for thermocapillary motion of deformable fluid particles, International Journal of Heat and Fluid Flow (2016), http://dx.doi.org/10.1016/j.ijheatfluidflow.2016.09.015

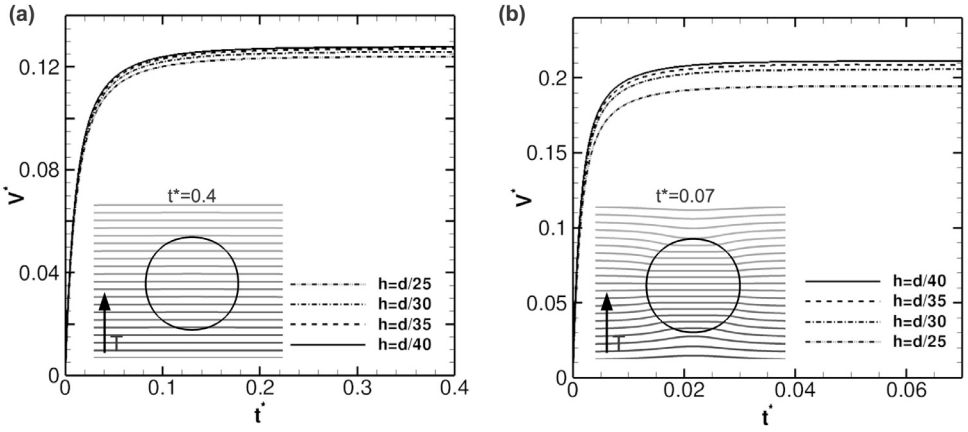

Fig. 8. Migration velocity versus time. (a) $Re = Ma = Ca = 0.06\bar{6}$, $\eta_\rho = \eta_\mu = \eta_{c_p} = \eta_\lambda = 1.0$. (b) $Re = Ma = 0.01$, $Ca = 0.016\bar{6}$, $\eta_\rho = \eta_\mu = \eta_{c_p} = \eta_\lambda = 0.5$.

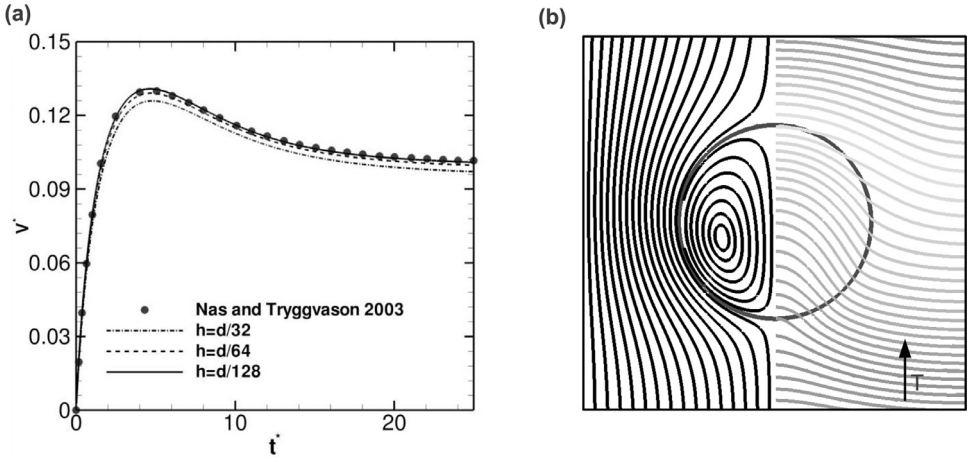

Fig. 9. $Re = 5$, $Ma = 20$, $Ca = 0.01666$, $\eta_\rho = \eta_\mu = \eta_{c_p} = \eta_\lambda = 0.5$ (a) Migration velocity versus time. (b) Streamlines (left) and Isotherms (right) at $t^* = 25$, with $h = d/128$.

domain simulations compared with the theoretical migration velocity for the unbounded problem is probably due to the confinement effect. Thus, the proposed method to include variable surface tension in the framework of the finite-volume/level-set method (Balcázar et al., 2014) yields to stable results, consistent in accuracy with previous numerical results from the literature.

4.2.2. Thermocapillary migration with finite Marangoni number

As further validation for thermocapillary migration with finite Marangoni number, the level-set model is used to solve a 2D test case introduced by Nas and Tryggvason (2003). The material property ratios η_ρ, η_μ, η_{c_p} and η_λ are set to 0.5, whereas the nondimensional parameters are chosen as $Re = 5$, $Ma = 20$, and $Ca = 0.016\bar{6}$. The computational domain is a rectangle extending $4d$ in the x direction and $8d$ in the y direction, where d is the drop diameter. The drop is initially located to the distance d above the bottom wall, on the vertical symmetry axis of the rectangular domain. The top and bottom walls are no-slip boundaries with constant temperature, and the horizontal boundaries are periodic.

Fig. 9a presents the migration velocity of the droplet versus time, computed by means of the present method, on uniform cartesian meshes with 64×128 ($h = d/32$), 128×256 ($h = d/64$) and 256×512 ($h = d/128$) grid points. Fig. 9b shows the streamlines and temperature contours at the time $t^* = 25$. It is observed that V^* converges with mesh refinement, whereas the difference in V^* calculated with $h = d/128$ and $h = d/64$ using the present model, is below 1.2%. Hence, it is clear from the aforementioned results that present computations are in excellent agreement with front-tracking simulation reported by Nas and Tryggvason (2003).

Once the accuracy of the level-set model has been demonstrated by the previous benchmark case, a set of three-dimensional simulations are carried out in order to study the effect of Re and Ma on the thermocapillary migration of a fluid particle, for which analytical solutions or reference results are not available. First, the effect of grid size on the migration velocity and temperature field is studied for the most stringent cases $(Ma, Re, Ca) = (100, 5, 0.1)$ and $(Ma, Re, Ca) = (500, 40, 0.0416\bar{6})$, with physical property ratios $\eta_\rho = \eta_\mu = \eta_\lambda = \eta_{c_p} = 1$, as illustrated in Figs. 10 and 11, respectively. Mesh parameters used in present study are summarized in Table 2. It is observed that numerical results converge as the grid size (h) is reduced, moreover, results using meshes M_3 ($h = d/35$) and M_4 ($h = d/40$) are very close, thus the mesh M_3 is selected for discussion of next numerical simulations.

Fig. 12 shows the normalized migration velocity for a set of Marangoni numbers, i.e., $Ma = \{1, 10, 50, 100, 500\}$, at $Re = \{1, 5, 20, 40\}$, with physical property ratios equal to one. In addition, Fig. 13 illustrates the evolution of the temperature contours and vorticity contours at four instants of time, on the symmetry plane $z = 0$, for $Re = 40$, $Ma = 100$, $Ca = 0.0416\bar{6}$ and physical property ratios equal to one. For a fixed Reynolds number, the initial migration velocity increases at the same rate, for all the range of Marangoni numbers studied, as shown Fig. 12, which is consistent with results reported by Liu et al. (2012). When the thermocapillary convection is weak, i.e. $Ma < 10$, it is observed two stages for the time evolution of V^*: an initial accelerating stage and the

Please cite this article as: N. Balcázar et al., A level-set model for thermocapillary motion of deformable fluid particles, International Journal of Heat and Fluid Flow (2016), http://dx.doi.org/10.1016/j.ijheatfluidflow.2016.09.015

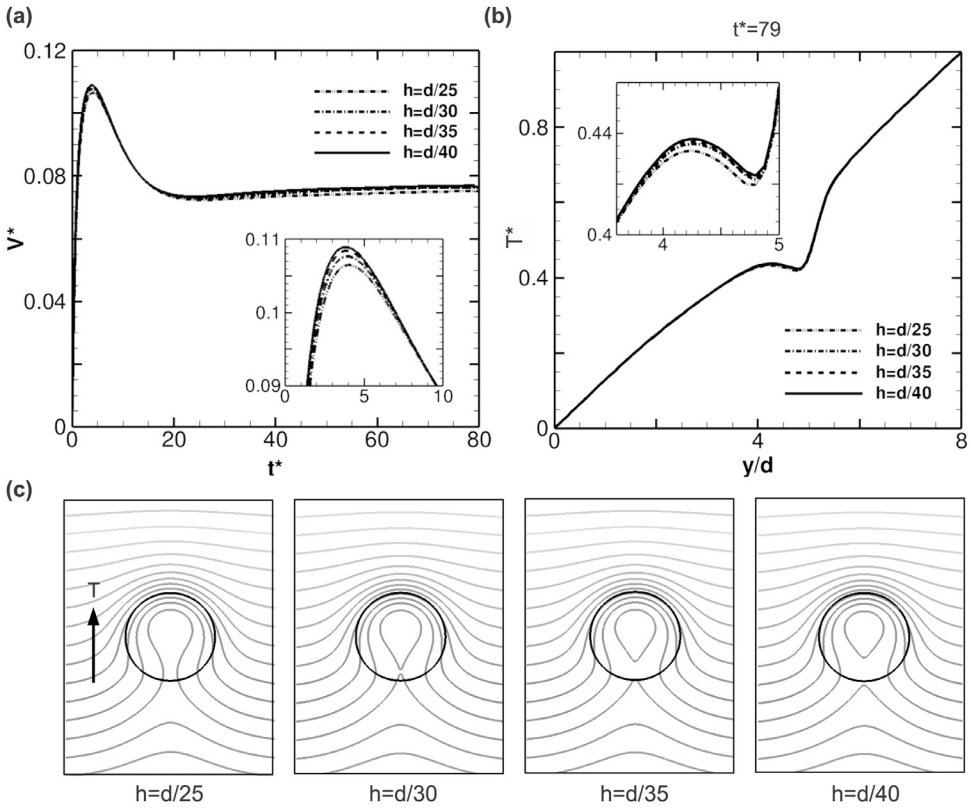

Fig. 10. Effect of the grid size (h), $Re = 5$, $Ma = 100$, $Ca = 0.1$, $\eta_\rho = \eta_\mu = \eta_{c_p} = \eta_\lambda = 1.0$, (a) Migration velocity. (b) Temperature on the symmetry line (y-axis) of the cylindrical domain ($t^* = 79$). (c) Isotherms on the symmetry plane $x - y$ ($t^* = 79$).

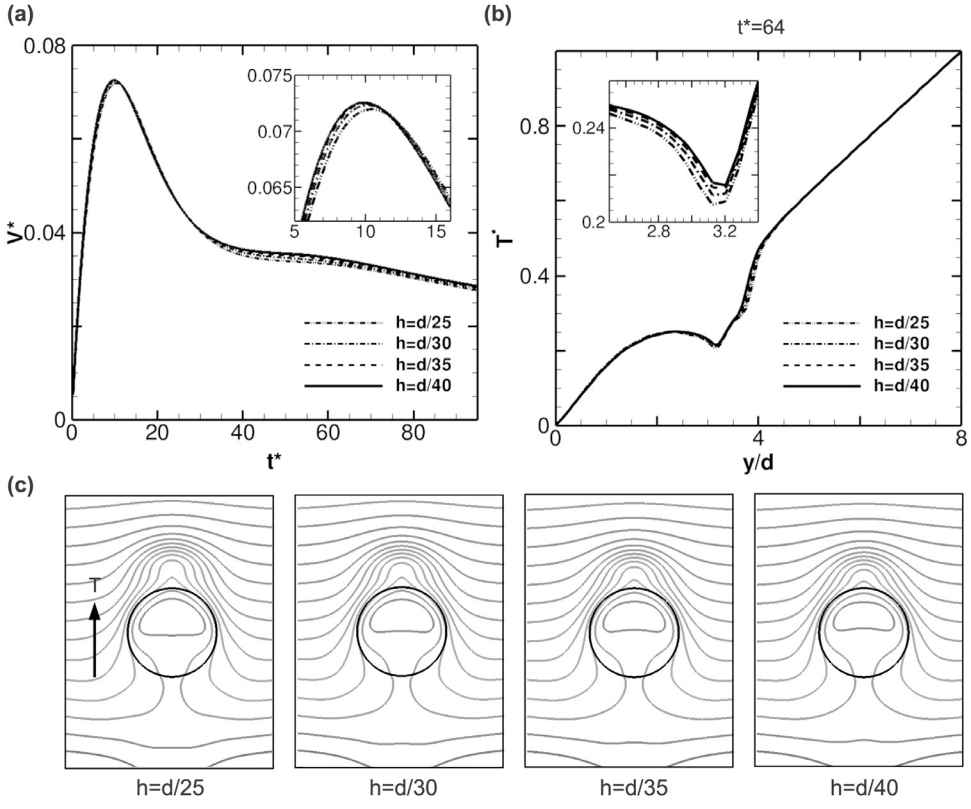

Fig. 11. Effect of the grid size (h), $Re = 40$, $Ma = 500$, $Ca = 0.0416\bar{6}$, $\eta_\rho = \eta_\mu = \eta_{c_p} = \eta_\lambda = 1.0$, (a) Migration velocity. (b) Temperature on the symmetry line (y-axis) of the cylindrical domain ($t^* = 64$). (c) Isotherms on the symmetry plane $x - y$ ($t^* = 64$).

Please cite this article as: N. Balcázar et al., A level-set model for thermocapillary motion of deformable fluid particles, International Journal of Heat and Fluid Flow (2016), http://dx.doi.org/10.1016/j.ijheatfluidflow.2016.09.015

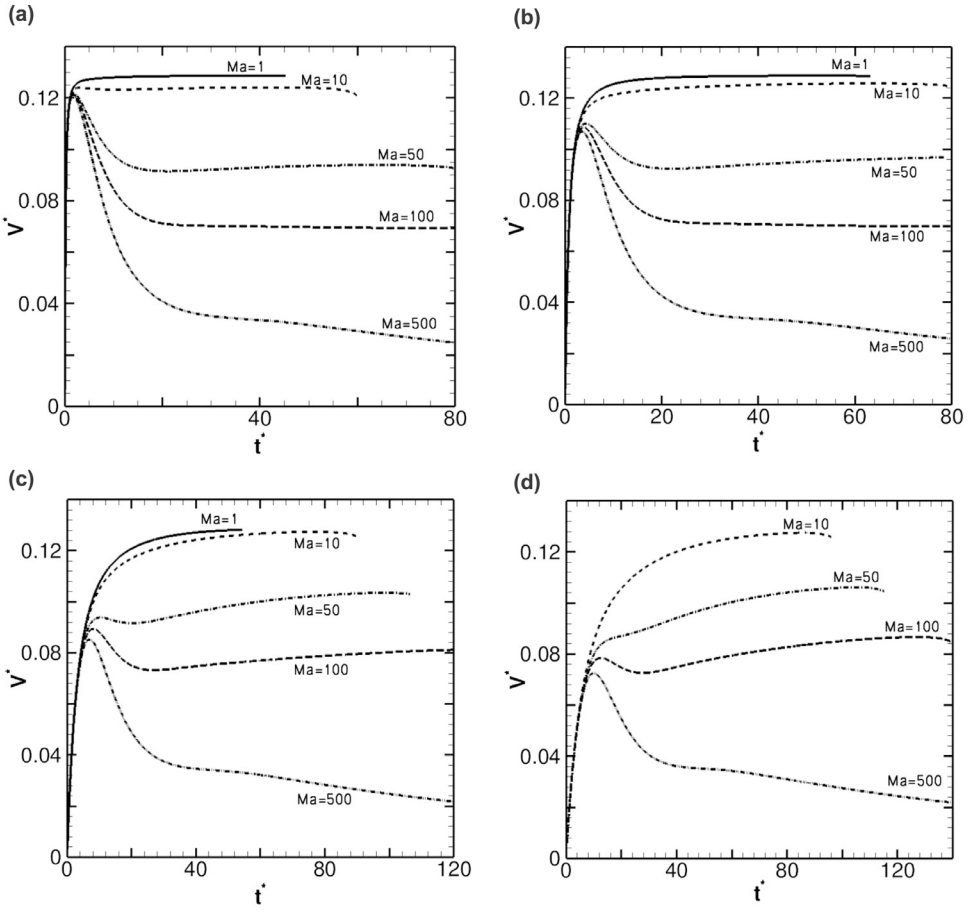

Fig. 12. Migration velocity versus time, $1 \leq Ma \leq 500$, $\eta_\rho = \eta_\mu = \eta_{c_p} = \eta_\lambda = 1.0$. (a) $Re = 1$, $Ca = 0.1$. (b) $Re = 5$, $Ca = 0.0416\bar{6}$. (c) $Re = 20$, $Ca = 0.0416\bar{6}$. (d) $Re = 40$, $Ca = 0.0416\bar{6}$.

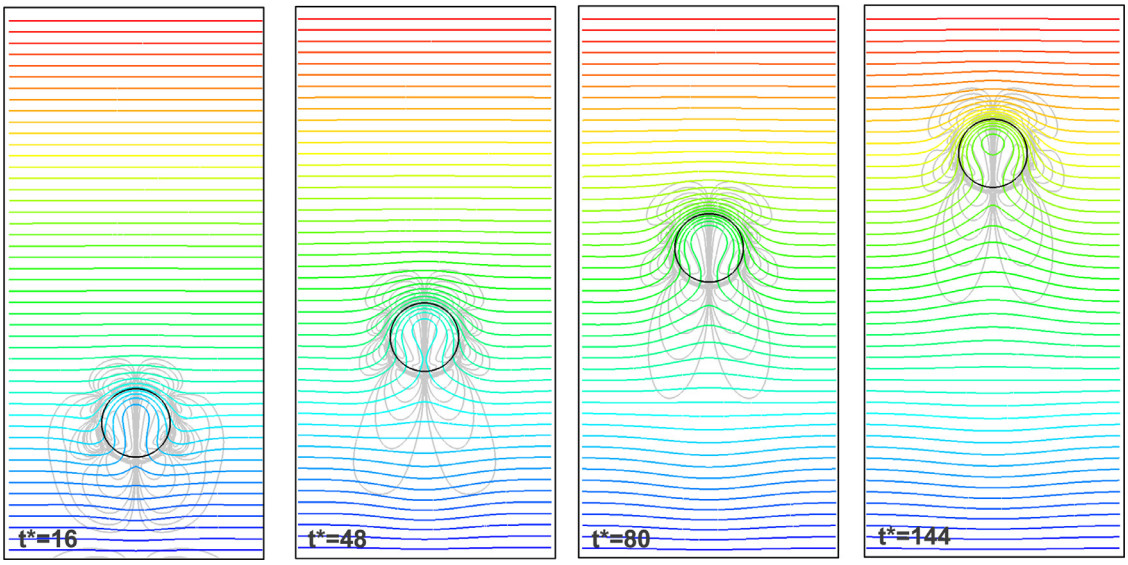

Fig. 13. Temperature and vorticity $((\nabla \times \mathbf{v}) \cdot \mathbf{e}_z)$ contours on the plane $z = 0$ for $Re = 40$, $Ca = 0.0416\bar{6}$, $Ma = \{100\}$, $\eta_\rho = \eta_\mu = \eta_{c_p} = \eta_\lambda = 1.0$.

final steady migration stage. As the thermocapillary convection is stronger, i.e. $Ma > 10$, there is an additional overshoot stage, which occurs at the beginning of the whole migration process because the influence of the thermal convection is major than that of the heat diffusion (Yin et al., 2008). Additionally, it is observed that V^* is a monotonically decreasing function of the Marangoni number, which is consistent with numerical findings reported by Yin et al. (2008) and Zhao et al. (2010). This dependence can be explained by means of the temperature contours illustrated in Figs. 14 and 15, where a redistribution of the temperature field inside the fluid particle is observed, because the velocity field is strongly coupled with the temperature as Ma increases. Moreover, it is observed that the

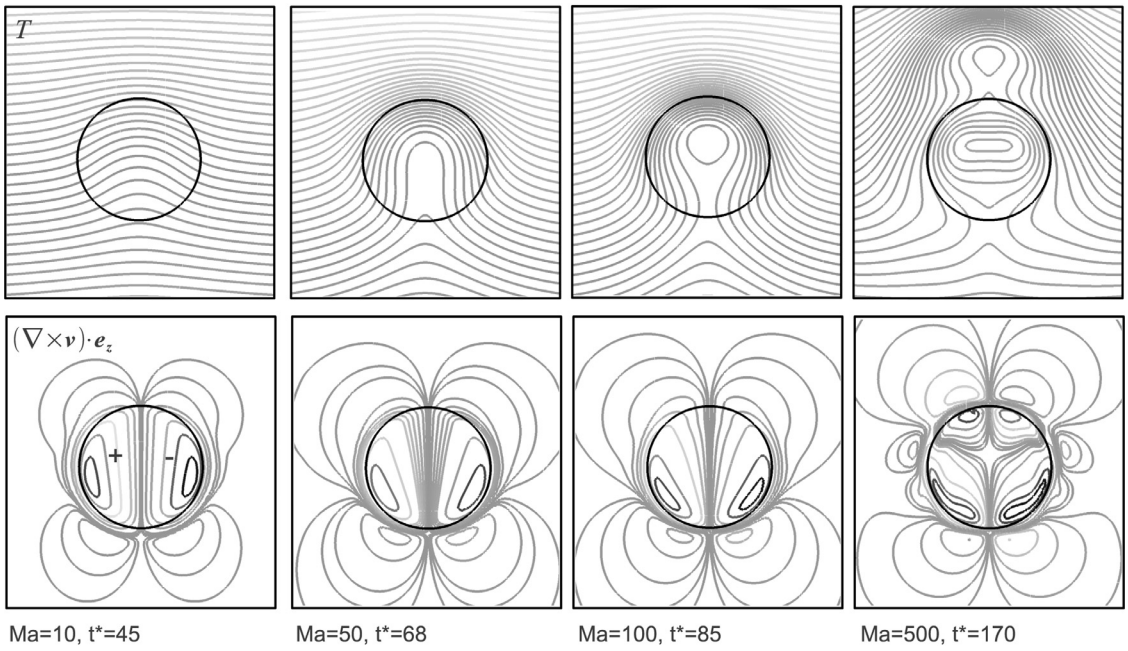

Fig. 14. Temperature and vorticity $((\nabla \times \mathbf{v}) \cdot \mathbf{e}_z)$ contours on the plane $z = 0$ for $Re = 5$, $Ca = 0.1$, $Ma = \{10, 50, 100, 500\}$, $\eta_\rho = \eta_\mu = \eta_{c_p} = \eta_\lambda = 1.0$.

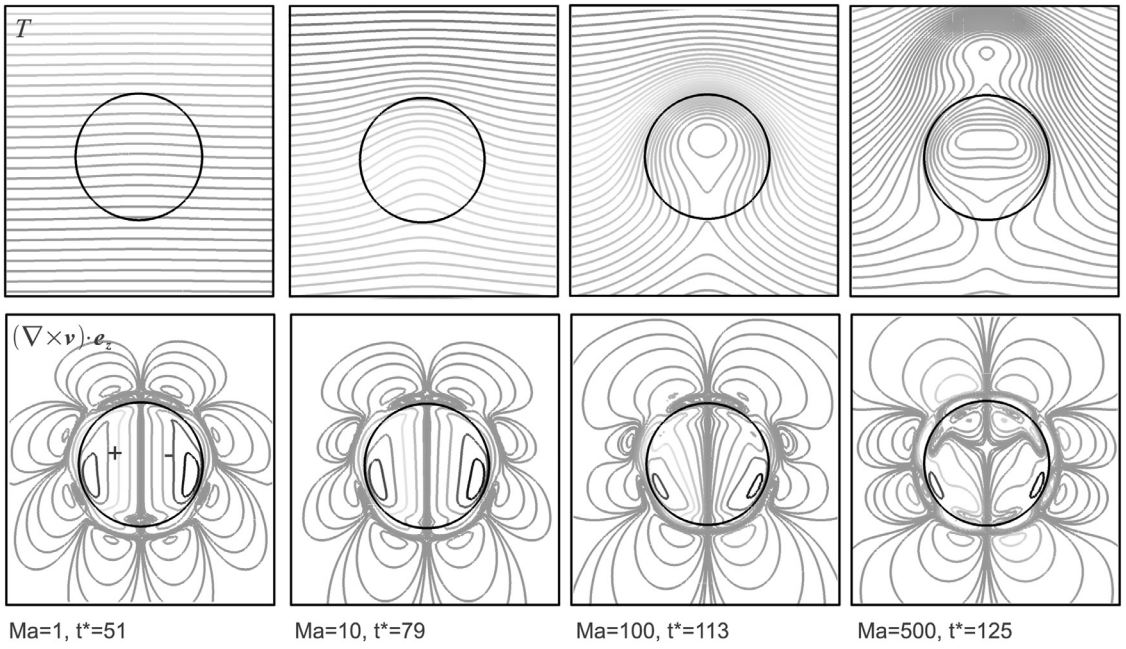

Fig. 15. Temperature and vorticity $((\nabla \times \mathbf{v}) \cdot \mathbf{e}_z)$ contours on the plane $z = 0$ for $Re = 20$, $Ca = 0.0416\bar{6}$, $Ma = \{1, 10, 100, 500\}$, $\eta_\rho = \eta_\mu = \eta_{c_p} = \eta_\lambda = 1.0$.

enhanced convective transport of energy, results in the wrapping of the temperature contours around the droplet interface, leading to a reduction of the temperature gradient at the surface. Indeed, a small average temperature gradient at the droplet interface leads to a reduction of the driving force for the droplet migration because the surface tension σ is a linear function of temperature, which explain the inverse relation between Ma and V^*.

The vorticity contours $(\mathbf{e}_z \cdot \nabla \times \mathbf{v})$ on the plane $z = 0$, indicate the presence of recirculation zones inside the droplets, as is illustrated in Figs. 14 and 15. The center position of these vortexes moves downstream with the increase of the Marangoni number, while at $Ma = 500$ additional recirculation zones are also observed inside the droplets. This fact can be explained by the corresponding temperature distributions which are depicted in Figs. 14 and 15. Hence, at low Marangoni number the temperature gradient is nearly uniform on the whole droplet interface, whereas a non uniform distribution of temperature gradient arises as the Ma increases, due that the temperature contours wrap around the interface. As consequence, a faster motion is induced in the zone with high temperature gradient, i.e., at the cold zone of the interface, in comparison with the induced motion at the warm region where temperature gradients are minor. Therefore, the vortexes inside the droplets are displaced downstream as Ma increases.

Moreover, Figs. 12–15 show that the unsteady thermocapillary migration of droplets depends of the Reynolds number. The most obvious difference happens at the beginning part of the simula-

Please cite this article as: N. Balcázar et al., A level-set model for thermocapillary motion of deformable fluid particles, International Journal of Heat and Fluid Flow (2016), http://dx.doi.org/10.1016/j.ijheatfluidflow.2016.09.015

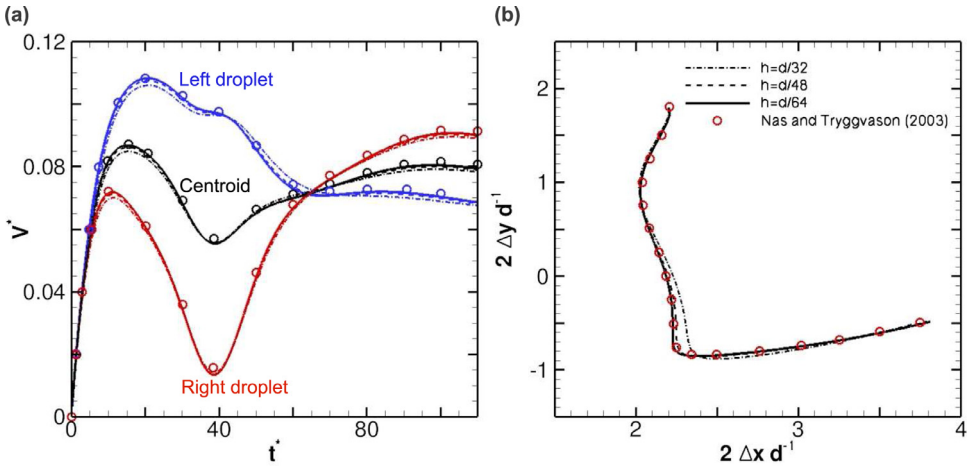

Fig. 16. Interaction of two droplets. $Re = 40$, $Ma = 40$, $Ca = 0.0416\bar{6}$, $\eta_\rho = \eta_\mu = \eta_{c_p} = \eta_\lambda = 0.5$. Lines for present numerical results ($h = \{d/32, d/48, d/64\}$), and symbols for results reported by Nas and Tryggvason (2003). (a) Migration velocity. (b) Vertical versus horizontal separation distance.

tions illustrated in Fig. 12, where it is clear that simulations with the smaller Reynolds number tend to move faster at the initial stage. These results can be explained because the tangential surface stresses can only be balanced by viscous stresses associated with fluid motion, as can be inferred from Eq. (5). It means, that the motion induced at the interface in the direction of increasing interfacial tension, lead to the motion of the fluids near to the interface, through the effect of viscosity. Moreover, the force driving the droplet is the counterforce of the viscosity force that arises from the aforementioned mechanism. Smaller values of Reynolds numbers mean larger viscosities, and the droplets will have larger acceleration. Indeed, for smaller *Re* the droplets can reach their maximum velocities within shorter periods of time, in comparison with the thermocapillary motion of droplets at larger values of *Re*.

4.3. Thermocapillary interaction of multiple droplets

In practical applications of thermocapillary flows, collections of fluid particles in bounded domains are frequently encountered. Thus, in order to validate the ability of the present method for simulating these systems, we solve the interaction effects between a pair of droplets, using the same simulation parameters reported by Nas and Tryggvason (2003). The ratio of material properties is $\eta_\rho = \eta_\mu = \eta_\lambda = \eta_{c_p} = 0.5$, with dimensionless parameters given by $Re = Ma = 40$ and $Ca = 0.0416\bar{6}$. The spatial domain Ω is a rectangle which extends $4d$ on the $x - axis$ and $8d$ on the $y - axis$. Ω is discretized by means of uniform cartesian meshes of $\{192 \times 384, 128 \times 256, 256 \times 512\}$ grid points, which are equivalent to the grid sizes $h = \{d/32, d/48, d/64\}$, respectively. The initial position of the droplet centroids are $(x/d, y/d) = (0.95, 2.0)$ for the right droplet, and $(x/d, y/d) = (2.05, 2.9)$ for the left droplet, which are initially defined as circular cylinders of diameter d. Periodic boundary condition is used in the x direction, whereas the walls are treated as no-slip boundaries. Furthermore, constant temperatures T_t and T_b are fixed at the top and bottom boundaries, respectively, with $T_t > T_b$.

Fig. 16 a shows the migration velocity V^* versus the dimensionless time t^* of the right droplet, left droplet, and droplets centroid, furthermore, grid convergence is demonstrated using three grid sizes $h = \{d/32, d/48, d/64\}$. Lines are used to represent numerical results obtained by the present method, and symbols are used to denote the reference results taken from Nas and Tryggvason (2003). This plot shows that both droplets start with a rapid acceleration and deceleration stage, which lead to an overshoot in their migration velocities. After this stage, it is observed that the left droplet achieves a quasi-steady state at $t \geq 60$, whereas the right droplet continues its motion with a new acceleration stage at $t^* \geq 40$. Additionally, Fig. 16b shows the vertical separation distance of the droplets versus its horizontal separation distance. At the beginning, the horizontal separation is almost constant, while the vertical separation is progressively reduced. It means that the droplets approximate each other during their migration toward the hot wall, but their trajectories hardly deviate from a straight line. As consequence the droplets collide and then separate each other, while the horizontal separation increases faster than its vertical separation, which indicates that the droplets continue their migration in a side-by-side configuration. Fig. 16 shows that present results obtained by the conservative level-set method are in excellent agreement with front-tracking simulation reported by Nas and Tryggvason (2003).

Figs. 17 and 18 show the isotherms and vorticity contours ($\mathbf{e}_z \cdot \nabla \times \mathbf{v}$) during the thermocapillary interaction of the two droplets. Regarding the vorticity contours, Fig. 17 shows that two asymmetric thermocapillary vortices are formed inside each fluid particle due to the imbalance in the surface tension on the droplet interfaces. Moreover, the size and strength of the vortexes near the warm region of the fluid–fluid interface are major than on the cold region due that temperature gradients are higher in the warm zone, as illustrated for instance in Fig. 18 at $t^* = 16$. During the collision of the droplets, at $t^* \geq 32$, a pair of vortices with opposite signs are observed near the collision zone, which interact between them to lead the separation of the fluid particles as illustrated in Fig. 17 at $t^* = \{48, 64\}$.

Fig. 18 shows that at the beginning the isotherms of the whole flow field are straight, therefore, this large temperature difference along the droplet interfaces leads to a large driving force on the droplets. As the droplets move forwards, the isotherms wrap around the droplet interface, which reduce the temperature differences of both drops in comparison with those at $t = 0$, indeed, their velocities begin to decrease. Moreover, after that droplets start to interact, the left droplet accelerates in direction to the right droplet, leading to the motion of hot fluid between them until eventually the droplets touch each other. Because the present level-set model has been designed to allow for the collision of fluid particles, avoiding the numerical coalescence, any flow of continuous fluid between them is blocked. As consequence, the droplets move away from each other to continue their motion in side by side configuration. Thus, the aforementioned results are consistent with front-tracking simulations reported by Nas et al. (2006).

Please cite this article as: N. Balcázar et al., A level-set model for thermocapillary motion of deformable fluid particles, International Journal of Heat and Fluid Flow (2016), http://dx.doi.org/10.1016/j.ijheatfluidflow.2016.09.015

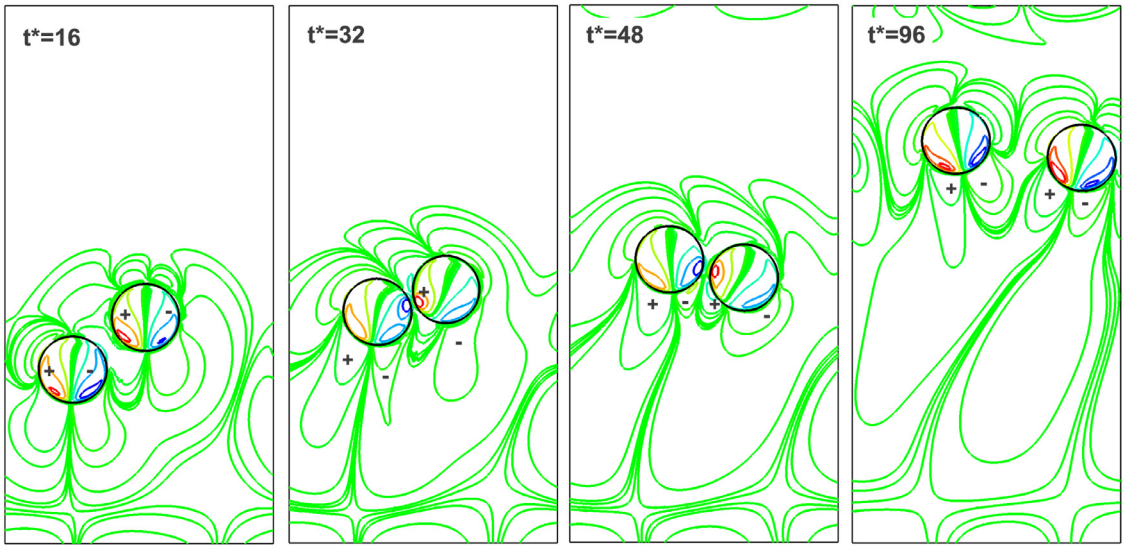

Fig. 17. Vorticity contours $((\nabla \times \mathbf{v}) \cdot \mathbf{e}_z)$ for the interaction of two drops. $Re = 40$, $Ma = 40$, $Ca = 0.0416\bar{6}$, $\eta_\rho = \eta_\mu = \eta_{c_p} = \eta_\lambda = 0.5$. Uniform cartesian mesh with $h = d/64$ or 256×512 grid points.

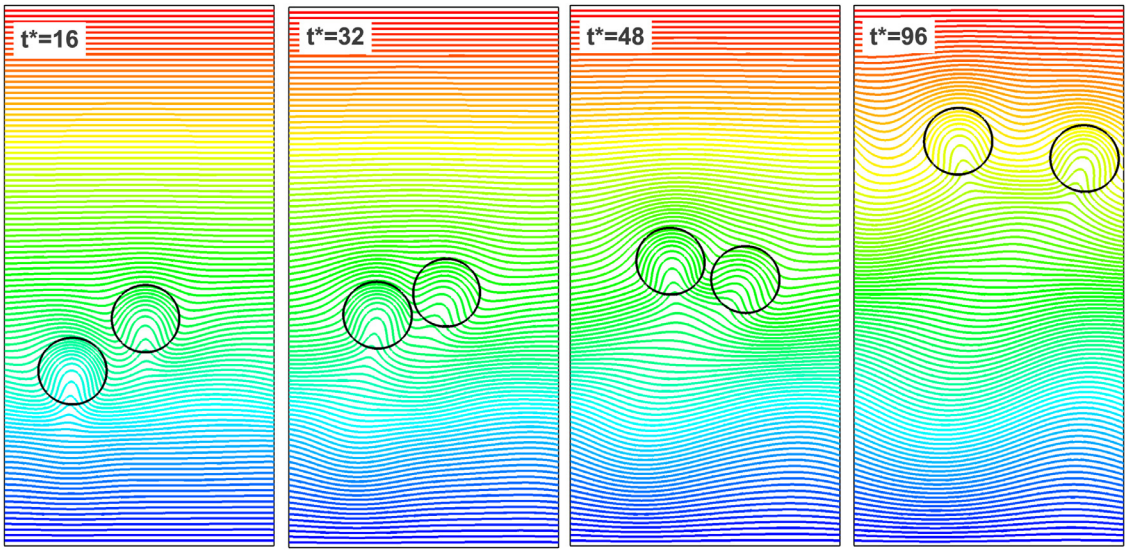

Fig. 18. Temperature contours for the interaction of two drops. $Re = 40$, $Ma = 40$, $Ca = 0.0416\bar{6}$, $\eta_\rho = \eta_\mu = \eta_{c_p} = \eta_\lambda = 0.5$. Uniform cartesian mesh with $h = d/64$ or 256×512 grid points.

With the confidence that the present model has been validated for the interaction of two droplets, now we study the three-dimensional interaction of multiple droplets in a rectangular channel which extends $6d \times 6d$ on the plane $x - z$, and $12d$ in the y axis. A swarm of 18 droplets are placed randomly in two layers of 9 droplets, close to the bottom wall, with a minimum distance droplet-wall of $2d$, and taken initially as spheres of diameter d. At the beginning, the fluids are quiescent and the temperature increases linearly from the bottom wall to the top wall, according to Eq. (47). Present simulations are performed using a uniform cartesian mesh of $240 \times 240 \times 480$ grid points, which is equivalent to the grid size $h = d/40$. All the wall boundaries are treated as no-slip, lateral walls (x and z directions) are adiabatic, whereas a constant temperature T_t and T_b is fixed at the top and bottom boundaries (y direction), respectively, with $T_t > T_b$. The physical parameters used in present $3D$ simulations are summarized in Table 5.

Figs. 19 and 20 illustrate the thermocapillary interaction of 18 droplets, with a set of isotherms and vorticity contours represented on the plane $z = 0$ for the physical parameters summarized in Table 5 (case A). It is observed that the first layer of 9 droplets separates of the second layer, which is closer to the bottom wall, and it moves ahead in direction to the warm wall, whereas the droplets in both layers align horizontally as they move across the channel. At the beginning, the trailing droplets (second layer) approach each other until eventually some of them collide, as illustrated in Figs. 19 and 20 ($t^* = 39.2$). Figs. 19 and 20 at $t^* = \{78.4, 117.6\}$ depict that the droplets are also dispersed in direction to the lateral walls, however they do not collide with them. Fig. 20 shows that counter-rotating thermocapillary vortices ($\mathbf{e}_z \cdot \nabla \times \mathbf{v}$) are formed inside each droplet, furthermore, vorticity

Table 5
Physical properties used in $3D$ simulations of multiple droplet interactions.

Case	Re	Ma	Ca	η_ρ	η_μ	η_λ	η_{c_p}
A	40	40	$0.0416\bar{6}$	0.5	0.5	0.5	0.5
B	20	60	$0.0416\bar{6}$	0.5	0.5	0.5	0.5

Please cite this article as: N. Balcázar et al., A level-set model for thermocapillary motion of deformable fluid particles, International Journal of Heat and Fluid Flow (2016), http://dx.doi.org/10.1016/j.ijheatfluidflow.2016.09.015

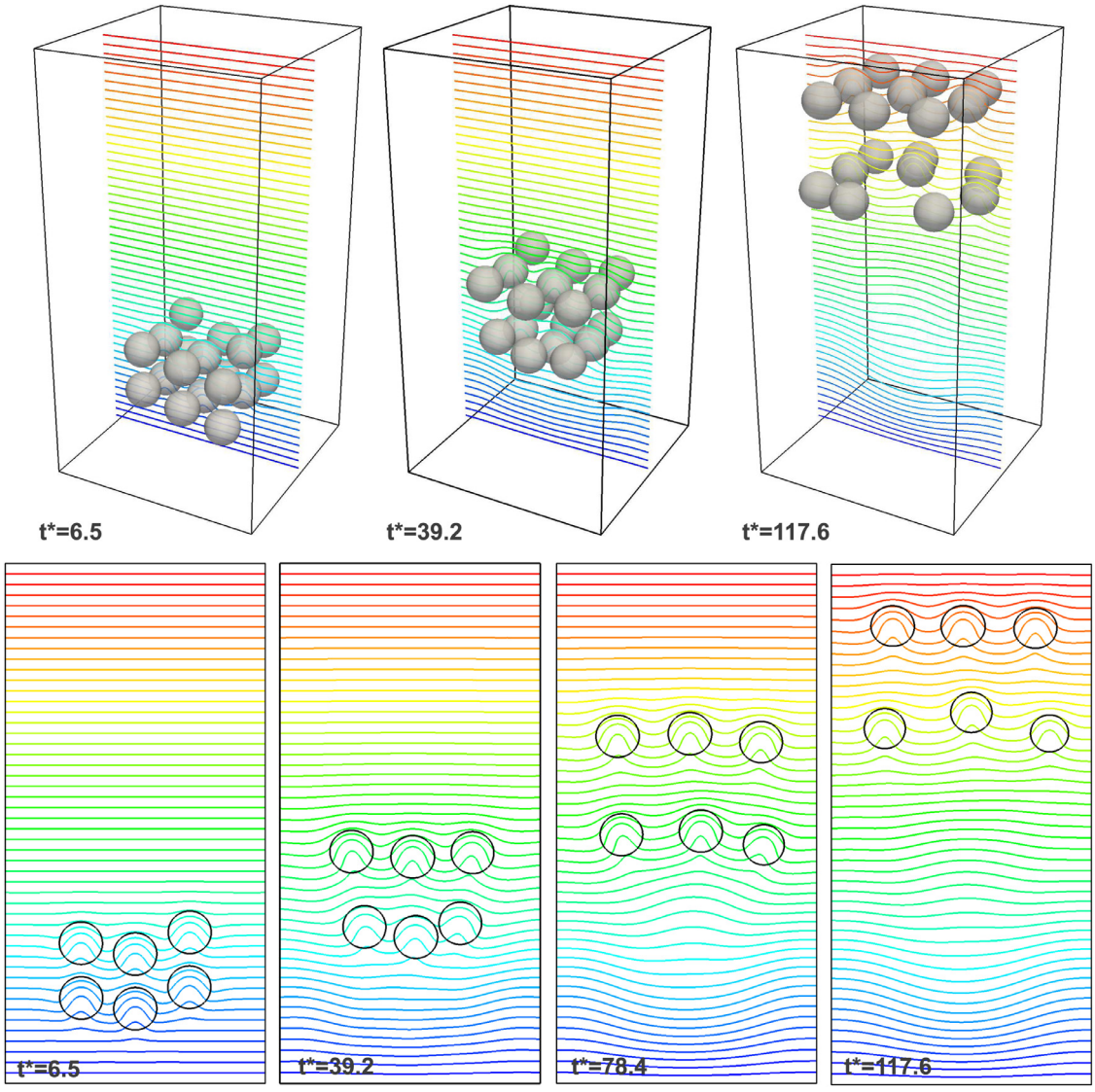

Fig. 19. $Re = 40,\ Ma = 40,\ Ca = 0.0416\bar{6},\ \eta_\rho = \eta_\mu = \eta_{c_p} = \eta_\lambda = 0.5,$ 18 droplets. Temperature contours at the plane $z = 0$.

is generated on the walls as the droplets approach to them, with opposite sign compared to the vorticity generated around the fluid particles. Inside the droplets, the cold fluid is pushed up, while the higher temperature fluid flows back between the droplets in order to conserve the mass, moreover, the isotherms wrap around the fluid–fluid interfaces and concentrate in front of the droplets, as shown Fig. 19.

Fig. 21 shows the migration velocity and vertical position of the droplets. Examining the velocity of each droplet in Fig. 21, it is clear that the velocity of the center of mass of the droplet swarm achieves a steady state, before the effect of the top wall arise, whereas each individual droplet presents oscillating migration velocities, for both cases summarized in Table 5. These oscillations are more evident for case B ($Re = 20,\ Ma = 60$), where the amplitude of the initial overshoot in the migration velocity is higher than case A ($Re = 40,\ Ma = 40$), which is consistent with the numerical findings described in Section 4.2.2. By moving in the direction of the temperature gradient, both the leading and trailing droplets form horizontal layers before they achieve the top wall, moreover, it is observed that the droplets of the top layer move faster than the droplets of the lower layer, indeed the vertical separation between the two layers increases as the time advances. Furthermore, the formation of these horizontal structures can be clearly inferred from the time evolution of the vertical locations of the droplets, which are depicted in Figs. 21b for both cases summarized in Table 5. These results are consistent with numerical findings reported by Nas et al. (2006) using the front-tracking method (Tryggvason et al., 2001).

These simulations demonstrate the feasibility of using the present multiple level-set approach to examine the dynamics of thermocapillary migration and interaction of multiple deformable droplets without numerical coalescence of the fluid particles. To the best of the authors' knowledge, these simulations have been affordable in the past only by means of the front-tracking method (Nas et al., 2006; Nas and Tryggvason, 2003; Tryggvason et al., 2001). On the other hand, in the framework of interface capturing methods (e.g. VOF or LS), the interaction of multiple interfaces when these are close enough, leads to the automatic coalescence of the fluid particles. Therefore, the aforementioned limitation of interface capturing methods is circumvented in the present model by means of the multiple marker approach (Balcázar et al., 2015a). In current implementation the CLS function of each fluid particle is computationally treated as one scalar field defined on the whole spatial domain Ω, indeed, the required memory storage and

Please cite this article as: N. Balcázar et al., A level-set model for thermocapillary motion of deformable fluid particles, International Journal of Heat and Fluid Flow (2016), http://dx.doi.org/10.1016/j.ijheatfluidflow.2016.09.015

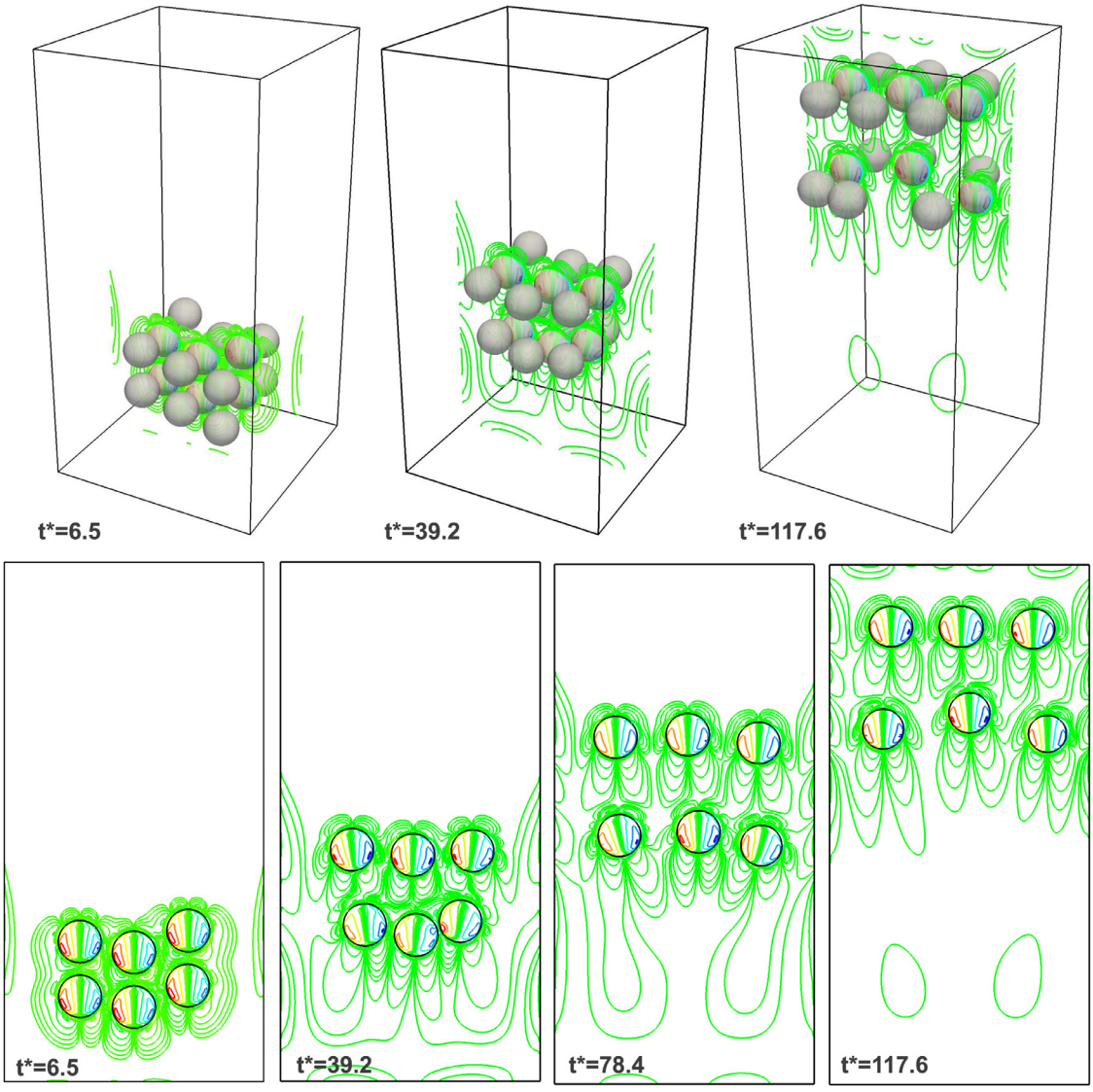

Fig. 20. $Re = 40$, $Ma = 40$, $Ca = 0.0416\tilde{6}$, $\eta_\rho = \eta_\mu = \eta_{c_p} = \eta_\lambda = 0.5$, 18 droplets. Vorticity contours, $(\nabla \times \mathbf{v}) \cdot \mathbf{e}_z$ at the plane $z = 0$.

computational effort associated with the interface representation scales with $n_b \times n_h$, where n_b is the number of fluid particles and n_h is the number of control volumes. Consequently, the simulation of thermocapillary interactions of multiple deformable droplets is practical for a relatively low number of fluid particles, less than $O(100)$ (Balcázar et al., 2015a).

5. Conclusions

In this paper, a new level-set model for thermal two-phase flows with variable surface tension has been introduced. The present model includes the Navier–Stokes equations for incompressible flows, with interfacial tension force and Marangoni stress modeled using the concept of continuum surface force (Brackbill et al., 1992). Interface capturing is performed by means of the CLS method presented in Balcázar et al. (2014, 2015b), whereas the multiple marker methodology introduced by Balcázar et al. (2015a), is used to avoid the numerical coalescence of the fluid–fluid interfaces, allowing for the collision of the fluid particles. Additionally, an energy equation is included to obtain temperature field, which is related to the surface tension by means of the equation of state. All governing equations have been discretized in the framework of the finite-volume method, according to the work introduced by Balcázar et al. (2014). To the best of the author's knowledge, this is the first time that thermocapillary effects in single and multiple droplets are modeled in the context of the conservative level-set method (Balcázar et al., 2014; 2015a; 2015b).

The proposed model is first validated against analytical solutions of thermal Poiseuille flow with constant surface tension, and thermocapillary driven convection in two superimposed fluids at negligible Reynolds and Marangoni numbers. It is then used to simulate thermocapillary motion of droplets, and its accuracy is further verified against the YGB theoretical predictions (Young et al., 1959) and numerical solutions from literature. As further validation, thermocapillary interaction of two droplets has been simulated, and present results compared with front-tracking simulations reported by Nas and Tryggvason (2003). Additionally, the effect of Reynolds and Marangoni numbers on the Marangoni migration of three-dimensional deformable droplets has been explored. As a challenging application, the thermocapillary interaction of multiple droplets in a confined channel has been performed. The aforementioned results demonstrate that the proposed level-set model is a reliable and accurate method for numerical simulation of thermocapillary flow. In future work, the present

Please cite this article as: N. Balcázar et al., A level-set model for thermocapillary motion of deformable fluid particles, International Journal of Heat and Fluid Flow (2016), http://dx.doi.org/10.1016/j.ijheatfluidflow.2016.09.015

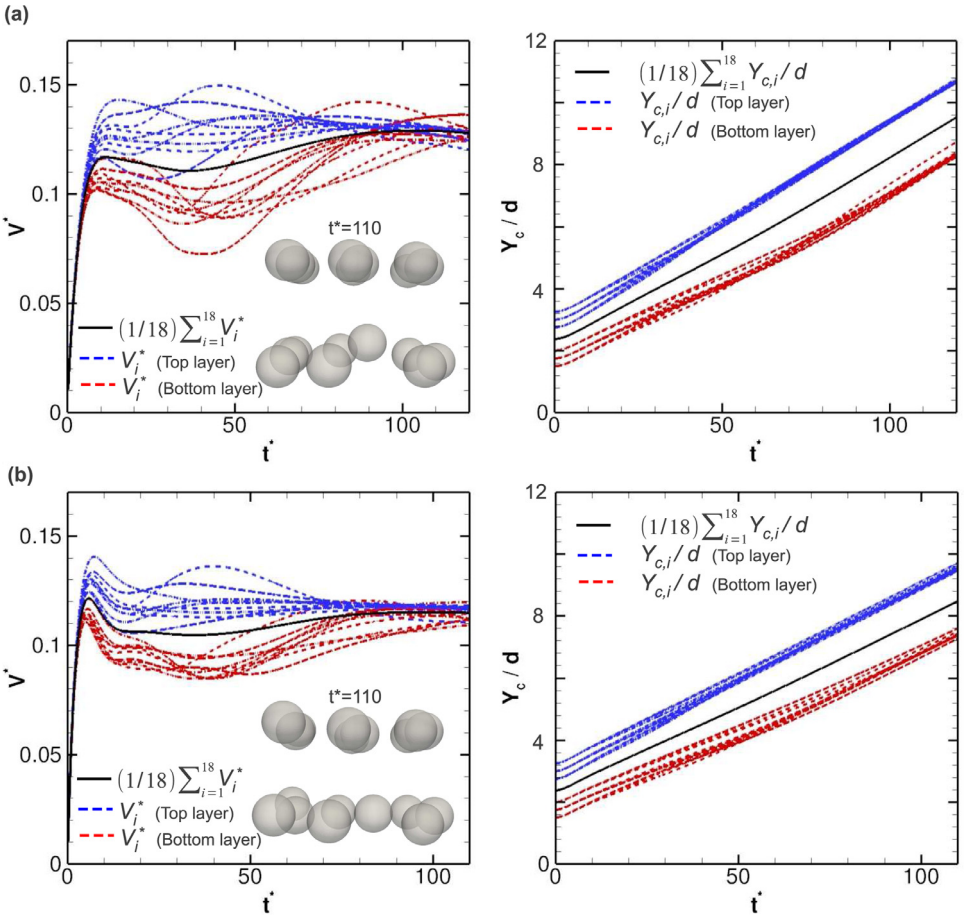

Fig. 21. Interaction of 18 droplets, $Ca = 0.0416\bar{6}$, $\eta_\rho = \eta_\mu = \eta_{c_p} = \eta_\lambda = 0.5$. Droplet velocity defined as $V_i^* = V_\Omega^{-1} \int_\Omega \phi_i \mathbf{v} \cdot \mathbf{e}_y dV$. Droplet centroid defined as $Y_{c,i}/d = d^{-1} V_\Omega^{-1} \int_\Omega \phi_i \mathbf{x} \cdot \mathbf{e}_y dV$, $i = 1, \ldots, 18$. (a) $Re = 40$, $Ma = 40$. (b) $Re = 20$, $Ma = 60$.

model could be extended to include surfactants and phase change phenomena.

Acknowledgments

This work has been financially supported by the Ministerio de Economía y Competitividad, Secretaría de Estado de Investigación, Desarrollo e Innovación, Spain (ENE2015-70672-P), and by Termo Fluids S.L. Néstor Balcázar acknowledges financial support of the Programa Torres Quevedo, Ministerio de Economía y Competitividad, Secretaría de Estado de Investigación, Desarrollo e Innovación (PTQ-14-07186), Spain. Three-dimensional simulations were carried out using computing time awarded by PRACE 10th Call (project 2014112666) on the supercomputer MareNostrum III based in Barcelona, Spain.

Appendix A. TVD flux limiter schemes

Total variation diminishing (TVD) differencing scheme used in present work has been introduced by Balcázar et al. (2014) in the context of unstructured grids, with the aim to avoid numerical oscillations and to minimize the numerical diffusion at the interface. Fig. 22 illustrates a stencil of three points $\{\mathbf{x}_{C'}, \mathbf{x}_{D'}, \mathbf{x}_{U'}\}$ on the line l_f, which is perpendicular to the face f on the face centroid $\mathbf{x}_f$. Points $\mathbf{x}_C$ and $\mathbf{x}_D$ refer to the upwind cell centroid and downwind cell centroid respect to the face f, whereas $\mathbf{x}_U$ is the far-upwind cell centroid. The point $\mathbf{x}_U$ is the closest cell-centroid to the point $\mathbf{x}_{U'} = \mathbf{x}_{C'} - \Delta\mathbf{x}_{C'D'}$, selected from the set of cell-centroids adjacent to the cell C in upwind direction with respect to the face f.

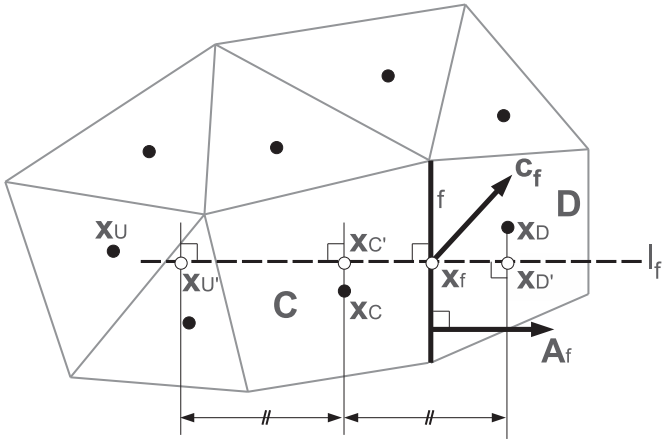

Fig. 22. Node stencil used for unstructured TVD flux limiter schemes, where $\mathbf{c}_f = \{\mathbf{v}_f, \mathbf{n}_f\}$.

Since physical variables ψ and their gradients $\nabla\psi$ are computed at cell centroids $\{\mathbf{x}_U, \mathbf{x}_C, \mathbf{x}_D\}$, it is possible to calculate their values at the points of the node-stencil $\{\mathbf{x}_{U'}, \mathbf{x}_{C'}, \mathbf{x}_{D'}\}$ by means of a first-order Taylor approximation, namely:

$$\begin{cases} \psi_{C'} = \psi_C + (\mathbf{x}_{C'} - \mathbf{x}_C) \cdot (\nabla\psi)_C, \\ \psi_{D'} = \psi_D + (\mathbf{x}_{D'} - \mathbf{x}_D) \cdot (\nabla\psi)_D, \\ \psi_{U'} = \psi_U + (\mathbf{x}_{U'} - \mathbf{x}_U) \cdot (\nabla\psi)_U. \end{cases} \tag{49}$$

Moreover, ψ_f is written as the sum of a diffusive first-order upwind part and an anti-diffusive term (Balcázar et al., 2014; Darwish and Moukalled, 2003; Lian-xia et al., 2008; Sweby, 1984)

$$\psi_f = \psi_{C'} + \frac{1}{2}L(\theta_f)(\psi_{D'} - \psi_{C'}) \tag{50}$$

The anti-diffusive part is multiplied by the flux limiter, $L(\theta_f)$, with θ_f defined as the upwind ratio of consecutive gradients of ψ:

$$\theta_f = \frac{\psi_{C'} - \psi_{U'}}{\psi_{D'} - \psi_{C'}} \tag{51}$$

Furthermore, the flux limiters used in this work have the forms:

$$L(\theta) \equiv \begin{cases} \max\{0, \min\{2\theta, 1\}, \min\{2, \theta\}\}, & \textit{TVD Superbee}. \\ (\theta + |\theta|)/(1 + |\theta|), & \textit{TVD Van} - \textit{Leer}. \\ 1, & \textit{Central difference}. \end{cases} \tag{52}$$

Recently Denner and van Wachem (2015b) and Hou et al. (2012) have reported a two-node distance weighting interpolation factor in place of the coefficient 1/2 in the anti-diffusive part of Eq. (50), with the aim to improve the aproximation of ψ at the face position on non-uniform unstructured grids. In the context of the present work, meshes have a constant grid size (h) in regions where the fluid-interface is present, moreover, the accuracy of Eq. (50) will increase with mesh refinement, whereas the factor 1/2 in Eq. (50) is exactly defined for uniform cartesian meshes. Another issue related to the design of TVD schemes on unstructured grids is the correction of mesh skewness (Denner and van Wachem, 2015b). In the framework of the present formulation, this problem is circumvented using a stencil of three virtual nodes $\{\mathbf{x}_{U'}, \mathbf{x}_{C'}, \mathbf{x}_{D'}\}$ located on the line l_f, which is orthogonal to the face f on the face centroid $\mathbf{x}_f$, as shown in Fig. 22.

Appendix B. Cell-face velocity interpolation

For the sake of completeness this section is devoted to obtain Eq. (32), which has been introduced in our previous work (Balcázar et al., 2014) in the context of isothermal and incompressible two-phase flows on collocated unstructured grids. This cell-face velocity ($\mathbf{v}_f$) is obtained in order to fulfill the incompressibility constraint and to maintain a strong pressure-velocity coupling on collocated meshes (Rhie and Chow, 1983). Thus, taking the divergence of Eq. (31), and integrating the resultant equation on the control volume Ω_P gives (Balcázar et al., 2014):

$$\sum_f \mathbf{v}_f^{n+1} \cdot \mathbf{A}_f = \sum_f \left(\mathbf{v}_f^* - \frac{\Delta t}{\rho_f}(\nabla_h p^{n+1})_f \right) \cdot \mathbf{A}_f \tag{53}$$

which can be reorganized as follows:

$$\sum_f \left(\mathbf{v}_f^{n+1} - \mathbf{v}_f^* + \frac{\Delta t}{\rho_f}(\nabla_h p^{n+1})_f \right) \cdot \mathbf{A}_f = 0 \tag{54}$$

Therefore, the coefficient of the sum in Eq. (54) can be used to define a cell-face velocity, $\mathbf{v}_f^{n+1}$, consistently with the incompressibility constraint as follows:

$$\mathbf{v}_f^{n+1} = \mathbf{v}_f^* - \frac{\Delta t}{\rho_f}(\nabla_h p^{n+1})_f \tag{55}$$

Now, $\mathbf{v}_f^*$ is interpolated as the weighting average of $\mathbf{v}_q^*$, where $q \in \{P, F\}$, P and F denote the adjacent cell nodes with a common face f:

$$\mathbf{v}_f^{n+1} = \sum_{q\in\{P,F\}} w_q \mathbf{v}_q^* - \frac{\Delta t}{\rho_f}(\nabla_h p^{n+1})_f \tag{56}$$

where w_q is defined as the weighting factor, such that $\sum_q w_q = 1$. Finally, Eq. (31) is replaced in Eq. (56) to obtain:

$$\mathbf{v}_f = \sum_{q\in\{P,F\}} w_q \left(\mathbf{v}_q^{n+1} + \frac{\Delta t}{\rho_q}(\nabla_h p^{n+1})_q \right) - \frac{\Delta t}{\rho_f}(\nabla_h p^{n+1})_f \tag{57}$$

or, in terms of the volume flux U_f:

$$\mathbf{v}_f \cdot \mathbf{A}_f = U_f = \sum_{q\in\{P,F\}} w_q \left(\mathbf{v}_q^{n+1} + \frac{\Delta t}{\rho_q}\left(\nabla_h p^{n+1}\right)_q \right) \cdot \mathbf{A}_f - \frac{\Delta t}{\rho_f}\left(\nabla_h p^{n+1}\right)_f \cdot \mathbf{A}_f \tag{58}$$

where

$$(\nabla_h p^{n+1})_f \cdot \mathbf{A}_f = (p_F^{n+1} - p_P^{n+1}) \frac{||\mathbf{A}_f||}{||\Delta \mathbf{x}_{P\to F}||} \tag{59}$$

Eq. (58) is similar to the momentum-weighted interpolation method introduced by (Felten and Lund (2006); Jofre et al. (2014)) for incompressible single-phase flows, and reported by (Denner and van Wachem (2014); Mencinger and Zun (2007)) in the context of incompressible two-phase flows. Moreover, following the work of Felten and Lund (2006), a weighting factor, $w_q = 0.5$, is used in Eq. (56), with the aim to minimize kinetic energy error on collocated curvilinear grids (Felten and Lund, 2006). This approximation leads to the cell-face velocity presented in Eq. (32). The reader is referred to Balcázar et al. (2014) for additional technical details on the finite-volume discretization of the governing equations on collocated unstructured grids.

Appendix C. Two-phase laminar forced convection

The thermal layered Poiseuille flow between two infinite walls driven by a constant pressure gradient, $((P_0 - P_L)/L_\Omega)\mathbf{e}_x$, is used for validation of the proposed level-set model, in the context of thermal two-phase flows with constant surface tension. The computational domain is $0 \leq x \leq L_\Omega$ and $-h_c \leqslant y \leqslant h_d$, while the interface is located at $y = 0$, as is illustrated in Fig. 2. The no-slip boundary condition is used on the top and bottom walls, a temperature T_t is applied at the top boundary while a temperature T_b is fixed on the bottom boundary, periodic boundary condition is used in the x direction. The effect of gravity is neglected and phase change does not take place. Moreover, there is not deformation of the interface and the surface tension is considered to be constant. Therefore, the analytical solution for the velocity and temperature fields can be obtained as (Zheng et al. (2016))

$$\mathbf{v}\cdot\mathbf{e}_x = \frac{(P_0 - P_L)h_0^2}{2\mu_c L_\Omega}\left(\frac{(1 + (h_d/h_c))h_d\mu_c}{\mu_c h_d + \mu_d h_c} + \left(\frac{(h_d/h_c)^2\mu_c - \mu_d}{(h_d/h_c)\mu_c + \mu_d} \right)\frac{y}{h_c} - \left(\frac{y}{h_c}\right)^2 \right) \tag{60}$$

$$T(x,y) = \frac{\lambda_d(T_t - T_b)}{\lambda_c h_d + \lambda_d h_c} y + \frac{\lambda_c h_d T_b + \lambda_d h_c T_h}{\lambda_c h_d + \lambda_d h_c} \tag{61}$$

in Ω_c, with $-h_c \leqslant y \leqslant 0$, and

$$\mathbf{v}\cdot\mathbf{e}_x = \frac{(P_0 - P_L)h_d^2}{2\mu_d L_\Omega}\left(\frac{(1 + (h_c/h_d))h_c\mu_d}{\mu_c h_d + \mu_d h_c} + \left(\frac{\mu_c - (h_c/h_d)^2\mu_d}{\mu_c + (h_c/h_d)\mu_d} \right)\frac{y}{h_c} - \left(\frac{y}{h_c}\right)^2 \right) \tag{62}$$

Please cite this article as: N. Balcázar et al., A level-set model for thermocapillary motion of deformable fluid particles, International Journal of Heat and Fluid Flow (2016), http://dx.doi.org/10.1016/j.ijheatfluidflow.2016.09.015

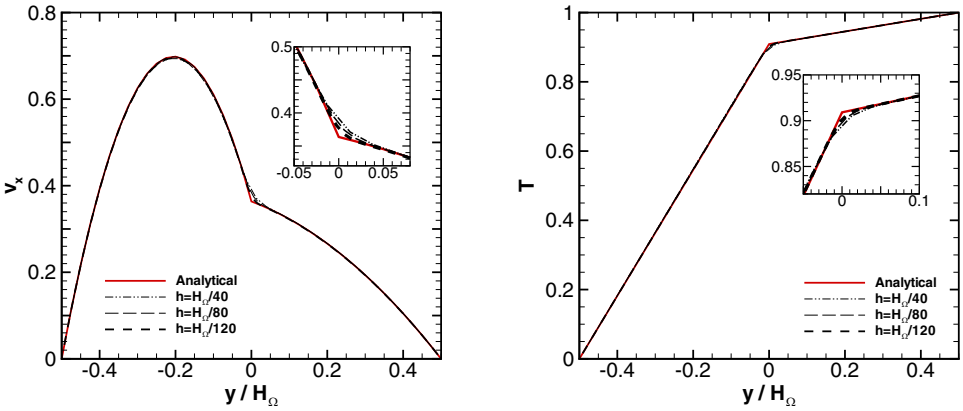

Fig. 23. Comparison of vertical velocity ($v_x = \mathbf{v} \cdot \mathbf{e}_x$) and temperature ($T$) on the line $x/H_\Omega = 0$. The interface is located at $y/H_\Omega = 0$.

Table 6
Physical properties used in simulation of two-phase laminar forced convection.

ρ_c	ρ_d	μ_c	μ_d	λ_c	λ_d	$c_{p,c}$	$c_{p,d}$	σ
1	1	0.10	0.01	0.1	0.01	0.1	0.1	24.5

$$T(x,y) = \frac{\lambda_c(T_t - T_b)}{\lambda_c h_d + \lambda_d h_c} y + \frac{\lambda_c h_d T_b + \lambda_d h_c T_h}{\lambda_c h_d + \lambda_d h_c} \tag{63}$$

in Ω_d, with $0 \le y \le h_d$.

Physical properties used in present simulation are summarized in Table 6. Wall temperatures are $T_h = 1$ and $T_c = 0$, whereas geometrical parameters are fixed to $L_\Omega \times H_\Omega = 4 \times 1$, with $h_c = h_d = 0.5H_\Omega$. Additionally, the applied external pressure gradient is $((P_0 - P_L)/L_\Omega)\mathbf{e}_x = 0.16\mathbf{e}_x$. The domain is discretized on a uniform cartesian mesh of 160×40 ($h = H_\Omega/40$), 320×80 ($h = H_\Omega/80$) and 480×120 ($h = H_\Omega/120$) grid points. At the time $t = 0$ both fluid layers are quiescent, whereas a linear profile is used as initial condition for temperature field. Present simulations have been performed for steady state, up to $t = 20$. Fig. 23 shows that numerical results for the temperature and velocity profiles are in excellent agreement with analytical solutions given by Eqs. (60)–(63). A slight difference is observed around the interface position because a continuous model has been used, however, this difference decreases with mesh refinement, as shown in Fig. 23. Present results are consistent with previous lattice-Boltzmann simulations reported by Zheng et al. (2016).

References

Anderson, J.L., 1985. Droplet interaction in thermocapillary motion. Int. J. Multiphase Flow 11, 813–824.
Balcázar, N., Jofre, L., Lehmkhul, O., Castro, J., Rigola, J., 2014. A finite-volume/level-set method for simulating two-phase flows on unstructured grids. Int. J. Multiphase Flow 64, 55–72.
Balcázar, N., Lehmkhul, O., Jofre, L., Rigola, J., Oliva, A., 2016. A coupled volume-of-fluid/level-set method for simulation of two-phase flows on unstructured meshes. Comput. Fluids 124, 12–29.
Balcázar, N., Lehmkhul, O., Rigola, J., Oliva, A., 2015. A multiple marker level-set method for simulation of deformable fluid particles. Int. J. Multiphase Flow 74, 125–142.
Balcázar, N., Lemhkuhl, O., Jofre, L., Oliva, A., 2015. Level-set simulations of buoyancy-driven motion of single and multiple bubbles. Int. J. Heat Fluid Flow 56, 91–107.
Brackbill, J.U., Kothe, D.B., Zemach, C., 1992. A continuum method for modeling surface tension. J. Comput. Phys. 100, 335–354.
Brady, P.T., Herrmann, M., Lopez, J.M., 2011. Confined thermocapillary motion of a three-dimensional deformable drop. Phys. Fluids 23, 022101.
Chang, Y.C., Keh, H.J., 2006. Thermocapillary motion of a fluid droplet perpendicular to two plane walls. Chem. Eng. Sci. 61, 5221–5235.
Chorin, A.J., 1968. Numerical solution of the Navier–Stokes equations. Math. Comput. 22, 745–762.
Darhuber, A.A., Troian, S.M., 2005. Principles of microfluidic actuation by modulation of surface stresses. Annu. Rev. Fluid Mech. 37, 425–455.
Darwish, M.S., Moukalled, F., 2003. TVD schemes for unstructured grids. Int. J. Heat Mass Transfer 46, 599–611.
Deen, N.G., Kuipers, J.A.M., 2013. Direct numerical simulation of wall to liquid heat transfer in dispersed gas–liquid two-phase flow using a volume of fluid approach. Chem. Eng. Sci. 102, 268–282.
Denner, F., van Wachem, B., 2014. Fully-coupled balanced-force VOF framework for arbitrary meshes with least-squares curvature evaluation from volume fractions. Numer. Heat Transfer Part B-Fundamentals 65, 218–255.
Denner, F., van Wachem, B., 2015. Numerical time-step restrictions as a result of capillary waves. J. Comput. Phys. 285, 24–40.
Denner, F., van Wachem, B., 2015. TVD differencing on three-dimensional unstructured meshes with monotonicity-preserving correction of mesh skewness. J. Comput. Phys. 298, 466–479.
Felten, F.N., Lund, T.S., 2006. Kinetic energy conservation issues associated with the collocated mesh scheme for incompressible flow. J. Comput. Phys. 215, 465–484.
Gottlieb, S., Chi-Wang, S., 1998. Total variation dimishing runge-kutta schemes. Mathem. Comput. 67, 73–85.
Guo, Z., Lin, P., 2015. A thermodynamically consistent phase-field model for two-phase flows with thermocapillary effects. J. Fluid Mech. 766, 226–271.
Haj-Hariri, H., Shi, Q., Borhan, A., 1997. Thermocapillary motion of deformable drops at finite reynolds and marangoni numbers. Phys. Fluids 9, 845.
Hirt, C., Nichols, B., 1981. Volume of fluid (VOF) method for the dynamics of free boundary. J. Comput. Phys. 39, 201–225.
Hou, J., Simons, F., Hinkelmann, R., 2012. Improved total variation diminishing schemes for advection simulation on arbitrary grids. Int. J. Numer. Meth. Fluids 70, 359–382.
Jofre, L., Lehmkuhl, O., Ventosa, J., Trias, X., Oliva, A., 2014. Conservation properties of unstructured finite-volume mesh schemes for the Navier–Stokes equations. Numer. Heat Transfer, Part B: Fundamentals 65, 53–79.
Karbalaei, A., Kumar, R., Cho, H., 2016. Thermocapillarity in microfluidics-a review. Micromachines 7, 1–41.
Keh, H.J., Chen, P.Y., Chen, L.S., 2002. Thermocapillary motion of a fluid droplet parallel to two plane walls. Int. J. Multiphase Flow 28, 1149–1175.
Keh, H.J., Chen, S.H., 1990. The axisymmetric thermocapillary motion of two droplets. Int. J. Multiphase Flow 16, 515–527.
Keh, H.J., Chen, S.H., 1992. Droplet interactions in axisymmetric thermocapillary motion. J. Colloid Interface Sci. 151, 1–16.
Kothe, D.B., Rider, W.J., Mosso, S.J., Brock, J.S., 1996. Volume tracking of interfaces having surface tension in two and three dimensions. AIAA 96-0859, 25.
Lehmkuhl, O., Perez-Segarra, C.D., Soria, M., Oliva, A., 2007. A new parallel unstructured CFD code for the simulation of turbulent industrial problems on low cost PC cluster. In: Proceedings of the Parallel CFD 2007 Conference, pp. 1–8.
Lian-xia, L., Hua-sheng, L., Li-jian, Q., 2008. An improved r-factor algorithm for TVD schemes. Int. J. Heat Mass Transfer 51, 610–617.
Liu, H., Zhang, Y., Valocchi, A.J., 2012. Modeling and simulation of thermocapillary flows using lattice boltzmann method. J. Comput. Phys. 231, 4433–4453.
Maa, C., Bothe, D., 2011. Direct numerical simulation of thermocapillary flow based on the volume of fluid method. Int. J. Multiph. Flow 37, 1045–1058.
Mencinger, J., Zun, I., 2007. On the finite volume discretization of discontinuous body force field on collocated grid: Application to VOF method. J. Comput. Phys. 221, 524–538.
Meyyappan, M., Subramanian, R.S., 1987. Thermocapillary migration of a gas bubble in an arbitrary direction with respect to a plane surface. J. Colloid Interf. Sci. 115, 206–219.
Meyyappan, M., Wilcox, W.R., Subramanian, R.S., 1981. Thermocapillary migration of a bubble normal to a plane surface. J. Colloid Interf. Sci. 83, 199–208.
Muradoglu, M., Tryggvason, G., 2008. A front-tracking method for computation of interfacial flows with soluble surfactants. J. Comput. Phys. 227, 2238–2262.
Nas, S., Muradoglu, M., Tryggvason, G., 2006. Pattern formation of drops in thermocapillary migration. Int. J. Heat Mass Transfer 49, 2265–2276.

Please cite this article as: N. Balcázar et al., A level-set model for thermocapillary motion of deformable fluid particles, International Journal of Heat and Fluid Flow (2016), http://dx.doi.org/10.1016/j.ijheatfluidflow.2016.09.015

Nas, S., Tryggvason, G., 2003. Thermocapillary interaction of two bubbles or drops. Int. J. Multiph. Flow 29, 1117–1135.
Olsson, E., Kreiss, G., 2005. A conservative level set method for two phase flow. J. Comput. Phys. 210, 225–246.
Osher, S., Sethian, J.A., 1988. Fronts propagating with curvature-dependent speed: algorithms based on hamilton-jacobi formulations. J. Comput. Phys. 79, 175–210.
Patankar, S., 1980. Numerical Heat Transfer and Fluid Flow. Taylor & Francis, New York.
Pendse, B., Esmaeeli, A., 2010. An analytical solution for thermocapillary-driven convection of superimposed fluids at zero reynolds and marangoni numbers. Int. J. Thermal Sci. 49, 1147–1155.
Peskin, C.S., 1977. Numerical analysis of blood flow in the heart. J. Comput. Phys. 25, 220–252.
Prosperetti, A., 2002. Navier–Stokes Numerical Algorithms for Free-surface Flow Computations: An Overview. in: Drop Surface Interactions. Springer, p. 237.
Rhie, C.M., Chow, W.L., 1983. Numerical study of the turbulent flow past an airfoil with trailing edge separation. AIAA J. 21, 1525–1532.
Sadhal, S.S., 1983. A note on the thermocapillary migration of a bubble normal to a plane surface. J. Colloid Interf. Sci. 95, 283–285.
Samareh, B., Mostaghimi, J., Moreau, C., 2014. Thermocapillary migration of a deformable droplet. Int. J. Heat Mass Transfer 73, 616–626.
Subramanian, R.S., 1981. Slow migration of a gas bubble in a thermal gradient. AIChE J. 27, 646–654.
Subramanian, R.S., 1983. Thermocapillary migration of bubbles and droplets. Adv. Space Res. 3, 145–150.
Subramanian, R.S., Balasubramaniam, R., 2001. The Motion of Bubbles and Drops in Reduced Gravity. Cambridge University Press.
Sun, R., Hu, W.-R., 2002. The thermocapillary migrations of two bubbles in microgravity environment. J. Colloid Interface Sci. 225, 375–381.
Sussman, M., Puckett, E.G., 2000. A coupled level set and volume-of-fluid method for computing 3d and axisymmetric incompressible two-phase flows. J. Comput. Phys. 162, 301–337.
Sussman, M., Smereka, P., Osher, S., 1994. A level set approach for computing solutions to incompressible two-phase flow. J. Comput. Phys. 144, 146–159.
Sweby, P.K., 1984. High resolution using flux limiters for hyperbolic conservation laws. SIAM J. Numer. Anal. 21, 995–1011.
Tryggvason, G., Bunner, B., Esmaeeli, A., Juric, D., Al-Rawahi, N., Tauber, W., Han, J., Nas, S., Jan, Y.-J., 2001. A front-tracking method for the computations of multiphase flow. J. Comput. Phys. 169, 708–759.
Yin, Z., Chang, L., Hu, W., Li, Q., Wang, H., 2012. Numerical simulations on thermocapillary migrations of nondeformable droplets with large marangoni numbers. Phys. Fluids 24, 092101.
Yin, Z., Gao, P., Hu, W., Chang, L., 2008. Thermocapillary migration of nondeformable drops. Phys. Fluids 20, 082101.
Yin, Z., Li, Q., 2015. Thermocapillary migration and interaction of drops: two non-merging drops in an aligned arrangement. J. Fluid Mech. 766, 436–467.
Young, N.O., Goldstein, J.S., Block, M.J., 1959. The motion of bubbles in a vertical temperature gradient. J. Fluid Mech. 6, 350–356.
Zhang, X., Davis, R.H., 1992. The collision rate of small drops undergoing thermocapillary migration. J. Colloid Interface Sci. 152, 548–561.
Zhao, J.F., Li, Z.D., Li, H.X., Jing, L., 2010. Thermocapillary migration of deformable bubbles at moderate to large marangoni number in microgravity. Microgravity Sci. Technol. 22, 295–303.
Zheng, L., Zheng, S., Zhai, Q., 2016. Continuous surface force based lattice boltzmann equation method for simulating thermocapillary flow. Phys. Lett. 380, 596–603.

Please cite this article as: N. Balcázar et al., A level-set model for thermocapillary motion of deformable fluid particles, International Journal of Heat and Fluid Flow (2016), http://dx.doi.org/10.1016/j.ijheatfluidflow.2016.09.015